

Article

U-Pb Ages, O Isotope Compositions, Raman Spectrum, and Geochemistry of Cassiterites from the Xi'ao Copper-Tin Polymetallic Deposit in Gejiu District, Yunnan Province

Yuehua Zhao ¹, Shouyu Chen ^{1,2,*}, Yuqiang Huang ¹, Jiangnan Zhao ^{1,2}, Xiang Tong ³ and Xingshou Chen ³

¹ Faculty of Earth Resources, China University of Geosciences, Wuhan 430074, China; yuehuazhao@outlook.com (Y.Z.); hyq_person@163.com (Y.H.); zjn198402@163.com (J.Z.)

² State Key Laboratory of Geological Processes and Mineral Resources, China University of Geosciences, Wuhan 430074, China

³ Yunnan Tin Company Group, Gejiu 610000, China; TXYXJT123@163.com (X.T.); chenxs123@126.com (X.C.)

* Correspondence: sychen@cug.edu.cn

Received: 24 February 2019; Accepted: 28 March 2019; Published: 31 March 2019



Abstract: The Xi'ao Cu-Sn polymetallic deposit is located in the inner alteration zone of the Laoka granite. The ore bodies extend to 400 m in the granite rock and primarily occur with fluorite and potassic alterations. Two cassiterite samples of altered rock-type ore and one tourmaline vein-type ore in the Xi'ao Cu-Sn polymetallic deposit yielded U-Pb ages of 83.3 ± 2.1 Ma, 84.9 ± 1.7 Ma, and 84.0 ± 5.6 Ma, respectively. The Raman spectrum peak values of A_{1g} were shifted to a lower frequency, possibly due to the substitution of Sn with Nb, Ta, Fe, and Mn. Measured $\delta^{18}O$ values of cassiterite samples and calculated $\delta^{18}O_{H_2O}$ values for the ore-forming fluid indicate that the latter was mostly derived from magma. The high Fe and Mn abundances for cassiterite are consistent with those of hydrothermal origin. The Nb, Ta, and Ti contents indicate that cassiterites in the Xi'ao deposit likely formed in a metallogenic environment that was largely affected by granitic magmatism. Therefore, we conclude that the Xi'ao deposit is a magmatic hydrothermal deposit.

Keywords: cassiterite; U-Pb ages; O isotope; Raman spectrum; Xi'ao Cu-Sn deposit; Gejiu district

1. Introduction

Cassiterite is one of the main tin minerals that is widespread in tin deposits; it can precipitate from hydrothermal ore-forming fluids over a very broad range of P-T-X conditions, and it is resistant to metamorphism, hydrothermal alteration, weathering, and abrasion [1,2]. Hence, it is likely that cassiterite effectively preserves primary information about the trace and rare-earth element geochemistry of the ore-forming fluid, which can provide important information for studies on the genesis of ore deposits [1–7]. Cassiterite belongs to the rutile group ($M^{4+}O_2$). It generally has high U and low Pb contents in its crystal structure and a high Pb closure temperature (560–860 °C) [8]. In recent years, great progress has been made in the use of cassiterite to determine the metallogenic ages of Sn polymetallic deposits [7,9–17]. Yuan et al. [18] obtained in situ LA-ICP-MS U-Pb age data (159.9 ± 1.9 Ma) and ID-TIMS U-Pb age data (158.2 ± 0.4 Ma) from cassiterite in the Furong Sn polymetallic deposit. Zhang et al. [16] provided further evidence to constrain the timing of granitic magmatism and hydrothermal mineralization by using LA-MC-ICP-MS U-Pb dating to calculate ages for igneous zircon and hydrothermal cassiterite. Compared with the metallogenic ages obtained from

altered minerals, ages obtained directly from cassiterite can more accurately reflect the timing of ore deposit formation [7].

China is extremely rich in tin resources, possessing 32% of the world's total Sn resources [19]. The Gejiu tin polymetallic district in Yunnan is well known for its large tin reserves containing approximately 335.74 Mt of Sn ores, 357.11 Mt of Cu ores, and 400 Mt of Pb-Zn ores. In the past few decades, this tin district has been extensively studied. Dating is a powerful tool used to determine mineralization characteristics and understand the ore genesis process [9,20–22]. Attempts to date the mineralization of the Gejiu district have been primarily performed on hydrothermal minerals (^{40}Ar - ^{39}Ar ages of micas, Re-Os ages of molybdenites) [23–26], but in some cases, the ages of these minerals may be inconsistent or inaccurate (the ^{40}Ar - ^{39}Ar and K-Ar ages range from 43.49 ± 0.87 Ma to 87.5 ± 0.6 Ma) [24,25,27,28]. Thus, ages of ore minerals are still needed to provide precise constraints on the timing of mineralization processes.

In Gejiu district, the Xi'ao ore field, an altered granite-type Cu-Sn polymetallic deposit (containing > 10 Mt Sn + Cu [29]), has been discovered in the inner alteration zone of the western edge of the Laochang–Kafang granite. In this deposit, the granite–marble contact zones rarely contain skarn minerals, and the intensity and scale of the mineralization are substantially constrained by the wall rock alteration and spatial distribution of granite [29,30]. The genesis of this deposit remains unclear, and additional studies are needed. Currently, most studies of cassiterite in the Gejiu district have focused on its mineral typomorphic characteristics [31–34], and some studies have investigated the geochronology and geochemistry of cassiterites from the Gaosong and Laochang deposits (two ore fields in Gejiu district) [14,35,36]. However, few studies have been performed on cassiterites from Xi'ao deposit, especially for altered rock-type cassiterites.

In this paper, cassiterite samples were collected from altered rock-type and tourmaline vein-type ores in the Xi'ao Cu-Sn polymetallic deposit and studied to constrain the timing of tin mineralization and precipitation environment of cassiterite. Consequently, the mineralogy of cassiterites was investigated by cathodoluminescence (CL) imagery and Raman spectroscopy. The geochemical signatures and oxygen isotopes of these minerals were also analyzed by using electron microprobe analyzer (EPMA) and isotope ratio mass spectrometry (MAT 253). In addition, the U-Pb ages of cassiterites were also measured by LA-ICP-MS. These results provide further insights into ore genesis in the Xi'ao deposit and highlight the potential of using cassiterite as a monitor of hydrothermal processes.

2. Geological Setting

The Gejiu mining district is located in the southeastern region of Yunnan Province. Tectonically, the Gejiu tin polymetallic deposit is located at the junction of the Yangtze Craton and Cathaysia and Indochina blocks (Figure 1). This deposit represents an important part of the southeast Yunnan tin polymetallic belt [37,38]. Sedimentary sequences in Gejiu district comprise Cambrian to Quaternary rocks, but Cretaceous rocks are lacking because of episodic uplift/erosion associated with Indosinian and Yanshanian tectonic events. Most outcrops in the Gejiu area comprise carbonate rocks of the Triassic Gejiu Formation and fine-grained clastic sediments and carbonates of the Falang Formation, the former of which are the main ore-hosting rocks. Numerous faults are present in the area, including the North–Northeast- (NNE) trending Longchahe, Jiaodingshan, and Yangjiatian faults, as well as the Northwest- (NW) trending Baishachong fault and the North–South- (NS) trending Gejiu fault. The Gejiu fault divides the study area into its eastern and western sectors. The eastern area, which contains 90% of the tin reserves in the Gejiu district [38], is dominated by the Wuzhishan anticlinorium, which includes five ore deposit areas; from north to south, these areas are: Malage, Songshujiao, Gaosong, Laochang, and Kafang (Figure 1).

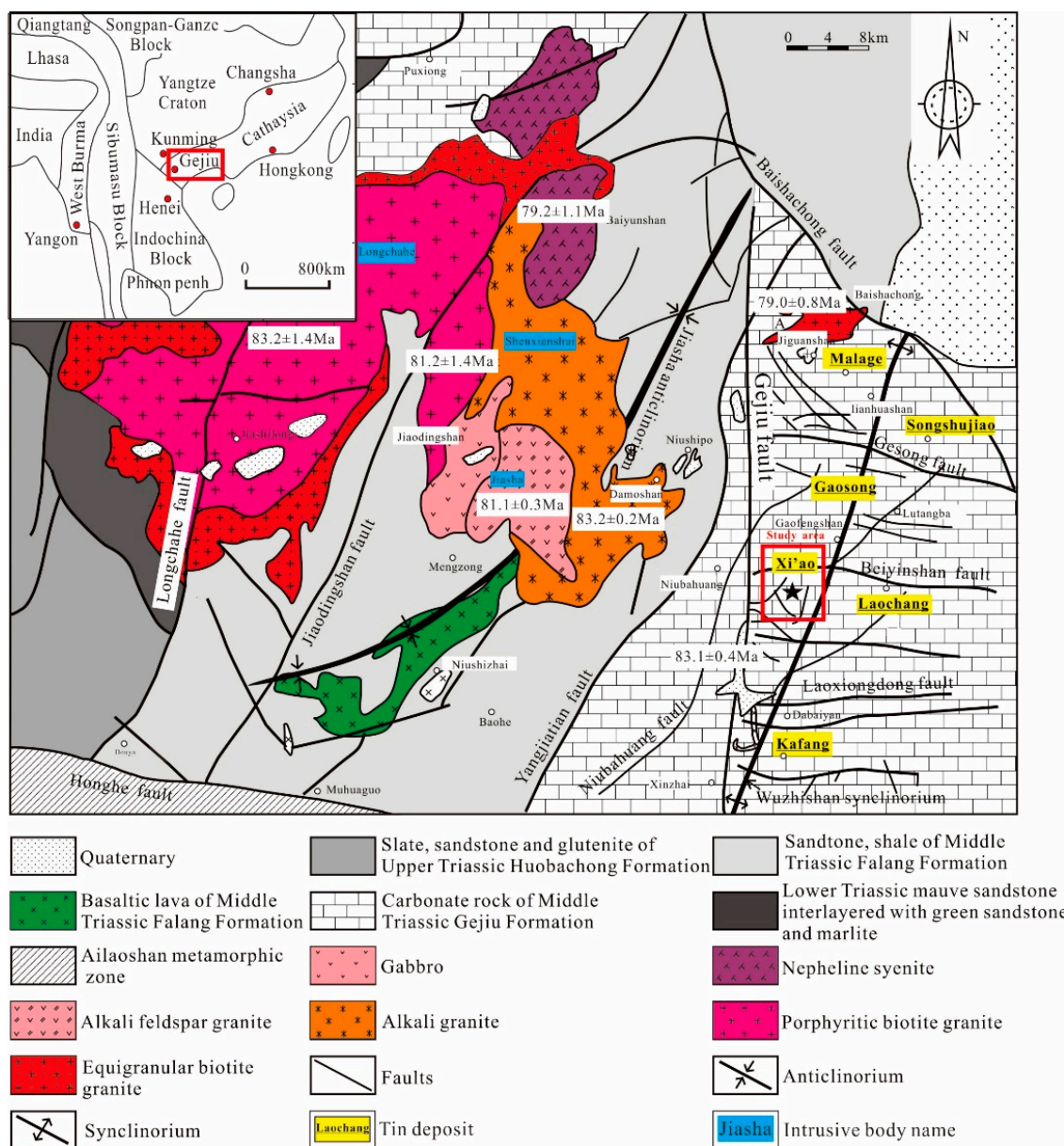


Figure 1. Geotectonic location (after [39]) and geological sketch map of Gejiu area, Yunnan Province (modified after [40]). The star shows the location of the Xi’ao Cu-Sn polymetallic deposit.

Frequent multistage magmatic activity occurred in the Gejiu area. Gejiu magmatic intrusions (emplacement ages are marked in Figure 1), which show a large variability, including gabbro, nepheline syenite, alkali feldspar granite, alkali granite, porphyritic biotite granite, and granular biotite granite, are widely exposed in the western area of Gejiu but are sparsely distributed in the eastern area. The ages of granites in Gejiu range from 53 Ma to 147 Ma according to dating obtained by different methods such as Ar-Ar/K-Ar, Rb-Sr, LA-ICP-MS/TIMS/SHRIMP (Sensitive High-Resolution Ion Microprobe) U-Pb, and Re-Os dating [24,25,41–45]. The latest chronological studies have shown that the magmatism in Gejiu district occurred during the late Cretaceous period (zircon U-Pb ages vary from 76.6 ± 3.6 Ma to 85.0 ± 0.85 Ma, Table 1). Trace elements and Sr-Nd-Hf isotopes demonstrate that the Gejiu granites were mainly derived from melting of continental crust in an intraplate environment [43]. The predominant granitoids and the synchronous mafic and ultramafic rocks in Gejiu thus constitute a bimodal magmatic association controlled by lithospheric extension and asthenosphere upwelling within the western Cathaysia block in Late Cretaceous [46–49], indicating a late Yanshanian intracontinental extensional

tectonic context [40,43,50,51]. Previous studies have also shown that the granites emplaced in Yanshanian are closely temporally and spatially related to the Gejiu tin polymetallic deposit [23,40,43].

Table 1. The ages of magmatic intrusions in Gejiu district.

Pluton Name	Lithology	Research Object	Dating Method	Age	Petrogenesis	Reference
Longchahe	Porphyritic biotite granite	biotite	K-Ar	100~115 Ma	A-type; peraluminous, alkaline granite	[51]
		whole rock	Rb-Sr	147 ± 3 Ma		[43]
		zircon	U-Pb	82.0 ± 0.3 Ma~83.2 ± 1.4 Ma		[43]
Masong	Porphyritic biotite granite	biotite	K-Ar	100~102 Ma	A-type and S-type; metaluminous—peraluminous, calc-alkaline granite	[51]
		K-feldspar	K-Ar	91.5~116 Ma		[51]
		whole rock	Rb-Sr	90.4 ± 6.3Ma		[43]
		zircon	U-Pb	82.8 ± 1.7 Ma		[43]
Shenxianshui	Equigranular granite	biotite	K-Ar	72~87 Ma	A-type; peraluminous, alkaline granite	[51]
		whole rock	Rb-Sr	84.4 ± 1.1 Ma		[43]
		zircon	U-Pb	81.0 ± 0.52 Ma~81.4 ± 0.4 Ma		[43]
Baishachong	Equigranular granite	biotite	K-Ar	53 Ma	Peraluminous, calc-alkaline granite	[52]
		whole rock	Rb-Sr	81.0 ± 2 Ma		[43]
		zircon	U-Pb	77.4 ± 2.5 Ma		[43]
Laoka	Equigranular granite	biotite	K-Ar	64 Ma~80 Ma	S-type; peraluminous, calc-alkaline	[52]
		whole rock	Rb-Sr	81.0 ± 4.9 Ma		[41]
		zircon	U-Pb	85.0 ± 0.85 Ma		[43]
	Porphyritic granite	zircon	U-Pb	83.3 ± 1.6 Ma		[43]
Baiyunshan	Alkali feldspar granite	biotite	K-Ar	59.5 Ma~62 Ma	/	[52]
		whole rock	Rb-Sr	94.3 ± 2.4 Ma		[53]
		zircon	U-Pb	76.6 ± 3.6 Ma		[53]
Jiasha	Gabbro	zircon	U-Pb	84.0 ± 0.6 Ma	/	[54]
Lamprophyre		zircon	U-Pb	77.2 ± 2.4 Ma	/	[53]

3. Ore Geology of the Xi'ao Deposit

The Xi'ao Cu-Sn polymetallic deposit is located in the western part of the Laochang ore field (Figure 1), and the mining area is approximately 25 km² [55]. The outcrop of the area mainly comprises Triassic Gejiu Formation carbonate rocks, which are the main ore-hosting rocks. The NW-trending Huangmaoshan and East–West- (EW) trending Wanzijie anticlines, which are the subsidiary anticlines of the Wuzhishan anticlinorium, are the main fold structures. The faults comprise three groups—NW-, NE-, and NS-trending—all of which are closely associated with mineralizations.

The Laoka equigranular biotite granite intruded into the Gejiu Formation in the Late Cretaceous (85.0 ± 0.85 Ma, [43]) at depths of 200–1800 m beneath the surface. It is mainly distributed in the Laochang and Kafang ore fields. Rock-forming minerals in equigranular biotite granite include K-feldspar (38%), plagioclase (25.2%), quartz (32.8%), and biotite (4%). The accessory minerals are zircon, apatite, titanite, allanite, monazite, tourmaline, and fluorite. Petrographic and geochemical features suggested that the hidden Laoka biotite granite has affinities of calc-alkaline S-type granite with higher contents of Sn (33.3 ppm), Cu (12.8 ppm), W (5.3 ppm), and mineralization-associated elements (F: 2500 ppm and Cl: 250 ppm) than normal granite [56,57]. It is peraluminous and enriched in silica and potassium (SiO₂ content is high, SiO₂ > 74%; K and Na rich, K₂O + NaO = 7.19%, K₂O/Na₂O = 6.8; aluminum saturation, Al/(K₂O + Na₂O) = 1.83; low oxidation rate, Ox = FeO/(FeO + Fe₂O₃) = 0.46 and highly fractionated, DI = 85~95) [29,38]. In addition, this granite is highly evolved and fractionated and possibly formed during the late evolution stage of the Gejiu granite [43,51].

The ore bodies are located in the inner alteration zone along the western edge of the Laoka granite (Figure 2) approximately 1000 m below the surface [29]. These ore bodies are mainly controlled by the

EW-trending faults, occur as veins and lenticular bodies, and extend to 400 m into the granite. The grades of tin and copper range from 0.2% to 1.34% and from 0.3% to 3.0%, with metal contents of 127.6 and 69.8 thousand tons, respectively [50]. The alteration of rocks is intensive, and skarn is poorly developed in the ore field. The country rock alterations are potassic alteration, tourmalinization, fluoritization, pyritization, silicification, chloritization, and carbonatization. The alteration zone boundary is vague. The alteration zones are classified into two major types—potassic and epidote-chlorite. The former is closely related to mineralization [56,58,59]. The mineral assemblages are listed in Table 2.

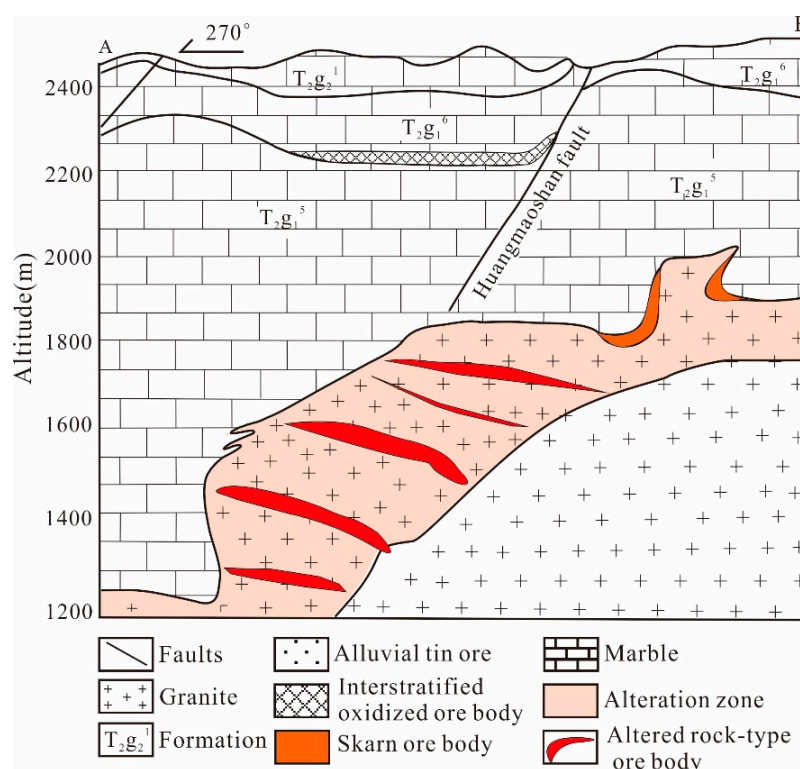


Figure 2. Mineral geological map of 164 exploration lines (after [29]).

Table 2. The mineral assemblage characteristics of altered-rock type ores in Xi’ao deposit.

Mineral Assemblage Type	Minerals	Ore Structure	Mineralization Significance
Potassium-fluoride-sulfide	K-feldspar, pyrite, chalcopyrite, and less fluorite, quartz, tourmaline, mica, etc.	Block, crumb, veinlet and disseminated	Big
Epidote and chlorite-pyritization-fluoride	Quartz, plagioclase, k-feldspar, biotite, epidote, chlorite, pyrite, fluorite, tourmaline, etc.	Veinlet and disseminated.	Small

Based on the occurrence, locality, and paragenesis of tin ore, two mineralization types were collected from the mining area, i.e., altered rock- and tourmaline vein-type ore (Figure 3).

Altered rock-type Sn polymetallic ore (Figure 3a,b) (due to the paucity of studies, we name it provisionally here) represents a newly discovered mineralization type, providing an interesting direction for deep prospecting in the future. The distribution of orebodies is controlled by EW-trending fractures, which are located in the inner alteration zone of the Laoka granite edge (approximately 10 m to 400 m within the rock mass). The main alteration types associated with mineralization are potassic alteration and chloritization. In the inner granite alteration zone, ore bodies are found only in K-altered granite. Orebodies mostly occur as veins, veinlets, or banded bodies such as parallel arrangements. When intersecting fractures, lenticular ores are also present. The average grade of Sn is 0.51 wt %,

and it can reach up to 10 wt %. In potassic alteration zone, the original plagioclase, quartz, and other minerals are overprinted and essentially replaced by secondary K-feldspar, perthite, and microcline. The main metallic minerals are chalcopyrite, pyrrhotite, sphalerite, cassiterite, pyrite, scheelite, and wolframite (Figure 3d,g). These minerals are mainly disseminated (rich), and stringers fill the structures (barren) of altered granite (Figure 3d,e). The gangue minerals mainly contain K-feldspar, fluorite, and tourmaline, and less mica, quartz, epidote, chlorite, and apatite. Ore textures are mainly metasomatic relict, poikilitic, and skeletal (Figure 3d,e).

Tourmaline vein-type ores (Figure 3c) occur as veins, veinlets, and stockwork and are predominantly controlled by fractures. The vein ores are present at a wide range of depths, from proximal to the granite to near the ground surface. The ore minerals, which are mainly disseminated, mainly contain chalcopyrite, pyrite, cassiterite, and arsenopyrite with lesser sphalerite and pyrrhotite (Figure 3h). The gangue minerals mainly include tourmaline and fluorite, with little quartz (Figure 3i).

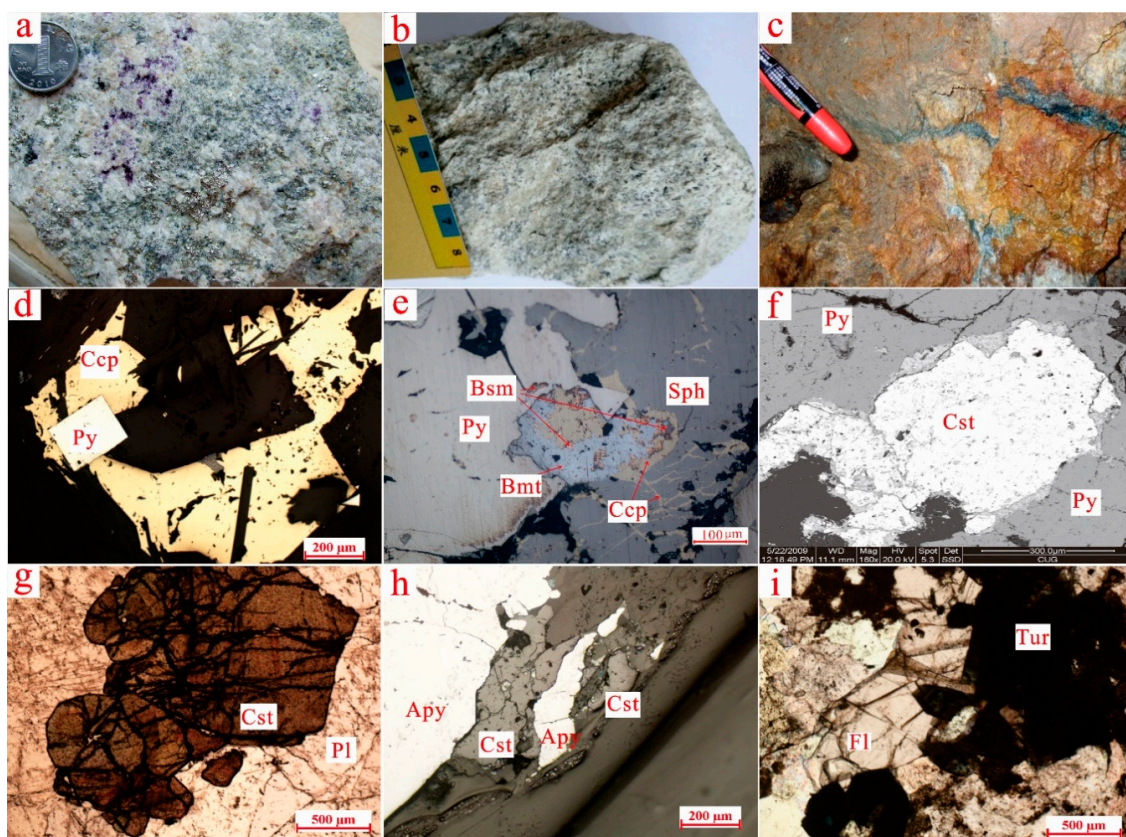


Figure 3. Photographs of tin ores from the Xi'ao Cu-Sn deposit; (a) is altered rock-type ore (XA-3) and mainly contains chalcopyrite, pyrite, sphalerite, quartz, fluorite, and cassiterite; (d) and (e) are photomicrographs of XA-3; (f) is the BSE image of XA-3; (b) is altered rock-type ore (XA-5) and mainly contains cassiterite, feldspar, and quartz; (g) is the photomicrographs of XA-5; (c) is tourmaline vein-type ore (XA-4) and mainly contains tourmaline, cassiterite, arsenopyrite, and fluorite; (h) and (i) is the photomicrographs of XA-4. Abbreviations: Ccp, chalcopyrite; Py, pyrite; Sph, sphalerite; Bsm, Bismuth; Bmt, bismuthinite; Cst, cassiterite; Pl, feldspar; Apy, arsenopyrite; Fl, fluorite; Tur, tourmaline.

4. Samples and Analytical Methods

Samples XA-3 (Figure 3a) and XA-5 (Figure 3b) were obtained from altered rock-type ore and tourmaline vein-type ore in the Xi'ao 1800 m adit, respectively. XA-4 (Figure 3c) was obtained from altered rock-type ore in granite at Fengliushan. Prior to analysis, samples were crushed, and cassiterite grains were separated using heavy liquid and magnetic separation techniques. They were then handpicked under a binocular microscope, mounted in an epoxy resin disc, and polished.

Cassiterite samples were examined carefully under the binocular microscope and scanning electron microscope to observe mineral and fluid inclusions and cracks. We chose the clean surface of cassiterites when experimenting in order to avoid fractures and inclusions, as common Pb is mostly associated with fluid inclusions [10].

Cathodoluminescence (CL) images of three cassiterite samples were obtained at Wuhan SampleSolution Analytical Technology Co., Ltd., Wuhan, China, using an analytical scanning electron microscope (JSM-IT100) (Japan Electron Optics Laboratory Co., Ltd., Tokyo, Japan) connected to a GATAN MINICL system (Gatan, Inc., Pleasanton, CA, USA). The operating conditions included an accelerating potential of 10 kV, a temperature of 20 °C, and an image acquisition time of 35 s/sheet. To compare the CL images of cassiterite grains, specific analytical conditions were adopted during the experiment such that the instrument automatically adjusted the parameters to obtain an image with the highest resolution after the scale was changed.

Raman spectra of three cassiterite samples were determined at the State Key Laboratory of Geological Processes and Mineral Resources (GPMA), China University of Geosciences (Wuhan), using a Renishaw RW-1000 Raman microspectrometer (Renishaw, London, UK). An argon ion laser with a wavelength of 514.5 nm was used for detection at 25 °C. The laser beam was focused on a small area measuring 2.0 μm. Working conditions: the laser power was 0.2 W, the collected time of Raman spectrum was 60 s, and the spectral resolution was ±1 nm⁻¹. The spectrograms were processed using OriginPro 8.0 (OriginLab, Northampton, MA, USA).

Mineral compositions were determined at the State Key Laboratory of Geological Processes and Mineral Resources, China University of Geosciences (Wuhan) using a JEOL JXA-8100 Electron Probe Micro Analyzer equipped with four wavelength-dispersive spectrometers (WDS) (Japan Electron Optics Laboratory Co., Ltd, Tokyo, Japan). The samples were first coated with a thin conductive carbon film prior to their analysis. The precautions suggested by Zhang and Yang [60] were used to minimize differences in the thicknesses of carbon films between samples and to obtain a uniform coating of approximately 20 nm. During the analysis of these minerals, an accelerating voltage of 15 kV, a beam current of 20 nA, and a spot size of 2 μm were used. Data were corrected online using a modified ZAF (atomic number, absorption, fluorescence) correction procedure. The peak counting time was 10 s for Sn, W, Ta, Si, Fe, and Nb, and 20 s for In, Ti, and Mn. The background counting time was one-half of the peak counting time on the high- and low-energy background positions. The following standards were used: cassiterite (Sn), tungsten (W), tantalum (Ta), olivine (Si), indium phosphide (In), pyrope garnet (Fe), niobium (Nb), rhodonite (Mn), and rutile (Ti). Analytical uncertainty was estimated at <1 wt % error for major elements and up to 5 wt % for trace elements.

Pure cassiterite separates were prepared for oxygen isotope analysis. The O isotope compositions were analyzed following the BrF₅ method [61]. The δ¹⁸O values of these separates were determined on a Finnigan MAT 253 ratio mass spectrometer (Thermo Fisher Scientific, USA). The O isotope results are reported relative to V-SMOW (Vienna standard mean ocean water), and the analytical precision is ±0.2‰ for δ¹⁸O. The degree of isotopic fractionation between cassiterite and water was calculated using Equation (1) [62] at the minimum trapping temperature, which was defined based on the average homogenization temperatures of the fluid inclusions in each quartz and calcite sample, as reported by Liao et al. [50]:

$$\delta^{18}\text{O}_{\text{water-SMOW}} = \delta^{18}\text{O}_{\text{V-SMOW}} - 10^3 \ln \alpha_{\text{cassiterite-water}} = \delta^{18}\text{O}_{\text{V-SMOW}} - (10.13 \times 10^6/T^2 - 26.09 \times 10^3/T + 12.58) \quad (1)$$

In situ U-Pb cassiterite dating was performed using a Neptune ICP-MS (Thermo Fisher Scientific ICAP Q) (Thermo Fisher Scientific, USA) coupled with an ESI 193 nm COHERENT Compex Pro 102F Excimer laser ablation system (Coherent Coherent Inc., Santa Clara, CA, USA) at the State Key Laboratory of Geological Processes and Mineral Resources, China University of Geosciences (Wuhan). The Squid smoothing device was used to reduce statistical error induced by laser ablation pulses and to improve the data quality [63,64]. Helium gas carrying the aerosol of the ablated sample was mixed with argon carrier gas and nitrogen as an additional di-atomic gas to enhance sensitivity before finally

flowing into the ICP. Typical gas flow settings for the Ar cooling gas, Ar auxiliary gas, and He carrier gas during the course of this study were 15 L/min, 0.75 L/min, and 0.86 L/min, respectively. The samples were analyzed using an energy density of 5 J/cm², a spot size of 32 μm, and a laser pulse frequency of 10 Hz. NIST SRM 610 (National Institute of Standards and Technology, Standard Reference Material 610) and an in-lab cassiterite standard AY-4 were used as external calibration standards. AY-4 was collected from the skarn orebody in the Anyuan tin deposit of the Furong orefield in the middle Nanling Range. This cassiterite sample has been well studied using ID-TIMS, and it has a U-Pb age of 158.2 ± 0.4 Ma [18]. Details can be found in Yuan et al. [13,18]. NIST SRM 610 was analyzed once after every ten analyses; AY-4 was analyzed twice after every five analyses. Each spot analysis incorporated approximately 20 s of background acquisition followed by 40 s of sample data acquisition. Isotopes were measured in time-resolved mode. For U-Pb dating, dwell times for each mass scan were 15 ms for ²⁰⁴Pb, ²⁰⁶Pb, ²⁰⁸Pb, ²³⁸U, and ²³⁵U, and 25 ms for ²⁰⁷Pb. Data errors of single spot were 1σ. Raw data reduction was performed off-line using ICPMSDataCal software (Liu Yongsheng, China University of Geosciences, China) [65,66]. The uncertainty of single populations, ratio uncertainty of the AY-4 reference material, and decay constant uncertainties were propagated to the ultimate results of the samples during the process of data reduction by ICPMSDataCal 10.1 [66]. Tera-Wasserburg concordia lower intercept age calculations were processed using Isoplot 3.0 (Kenneth R. Ludwig, United States Geological Survey, USA) [67].

5. Results

5.1. Color and CL Images

The typomorphic characteristics of the color of cassiterite have been well studied by researchers due to its easily recognized and distinguishable features [4,12,31–34,68].

As shown in Figure 4, the colors of the three cassiterite samples varied widely (e.g., black, dark brown, brown, red brown, light brown, gray, colorless). The colors of altered rock-type cassiterites varied from colorless to dark, while those of tourmaline vein-type cassiterites were mainly dark. In addition, the grain sizes of cassiterites that formed in the same ore-forming setting were uniform, while they varied widely among cassiterites of different genetic types, ranging from $n \times 10 \mu\text{m}$ to $n \times 100 \mu\text{m}$. The particle sizes of cassiterites from XA-3 (350 × 200 μm to 550 × 380 μm) and XA-4 (280 × 240 μm to 490 × 330 μm) were larger than those from XA-5 (130 × 110 μm to 270 × 180 μm).

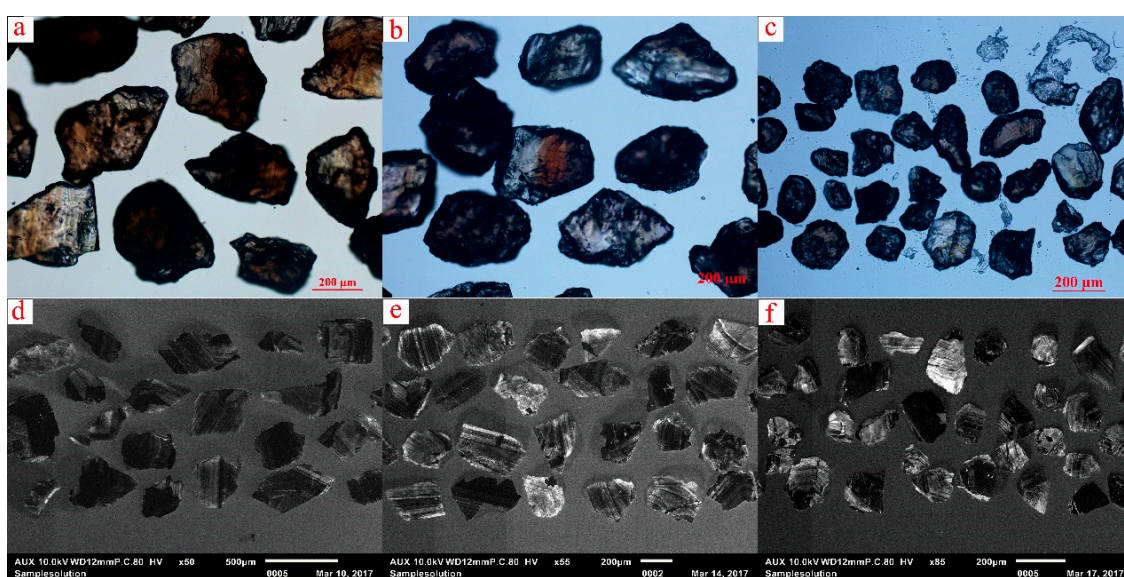


Figure 4. Photomicrographs and cathodoluminescence (CL) image of tin ores from the Xi'ao Cu-Sn deposit. XA-3: (a,d); XA-4: (b,e); XA-5: (c,f).

Pronounced differences in the luminescence and internal structures of CL images were observed among cassiterites that formed in different crystallization environments (Figure 5). Based on the luminescence and complexity of the internal structures observed in CL images, the cassiterites could be divided into two zones: (1) the H zone (homogeneous zone), which is characterized by black luminescence and homogeneous internal structures (Figure 5a,b,d), and (2) the O zone (oscillatory zone), which exhibits gray, off-white luminescence with some hourglass structures and oscillatory zoning (Figure 5a,b) and others homogeneous (Figure 5c,e). XA-3 cassiterites had both H and O units, and oscillatory zoning was common in O units. XA-4 cassiterites were predominantly composed of O units with no H units. XA-5 cassiterites were primarily composed of O units with oscillatory zoning and few H units.

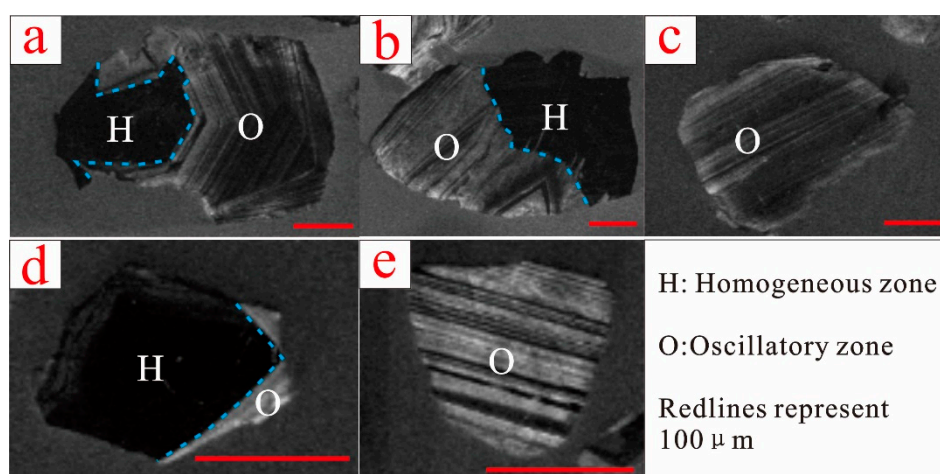


Figure 5. Representative CL images of cassiterites from different types of ores in the Xi'ao deposit. XA-3: (a,b); XA-4: (c); XA-5: (d,e).

5.2. Raman Spectrum

Cassiterite has a rutile structure with space group D_{4h}^{14} -P4/mnm ($Z = 2$). The tin atom is located in the octahedral coordination of oxygen. The mechanical representation of the normal vibration modes at the center of the Brillouin zone is given as $\Gamma = A_{1g} + A_{2g} + B_{1g} + B_{2g} + E_g + 2B_{1u} + A_{2u} + 3E_u$ [69,70], among which A_{1g} , B_{1g} , B_{2g} and E_g were assigned to Raman active while $A_{2g} + 2B_{1u}$ was assigned to Raman inactive.

The Raman spectra of Xi'ao cassiterite samples are shown in Figure 6. The most intense peak can be attributed to A_{1g} mode, which was found to shift to 633.693 cm^{-1} in XA-3, 632.295 cm^{-1} in XA-4 and 633.693 cm^{-1} in XA-4, while those exhibited at 473.355 cm^{-1} to 531.539 cm^{-1} and 774.156 cm^{-1} to 776.176 cm^{-1} may have been due to vibrational modes E_g and B_{2g} , respectively. B_{1g} mode was found to shift to 88.731 cm^{-1} in XA-3, 87.346 cm^{-1} in XA-4 and 85.058 cm^{-1} in XA-5. The Raman spectra peaks of cassiterites collected from Xi'ao are in good agreement with the pure SnO_2 Raman spectra peaks of $A_{1g} = 646 \text{ cm}^{-1}$, $B_{2g} = 752 \text{ cm}^{-1}$, $E_g = 441 \text{ cm}^{-1}$ and $B_{1g} = 100 \text{ cm}^{-1}$ reported by Katiyar et al. [71].

Additional peaks were observed at 438.109 in XA-3 and XA-5 and 233.004 in XA-4, which may have been due to the nano-inclusions, possibly requiring further study.

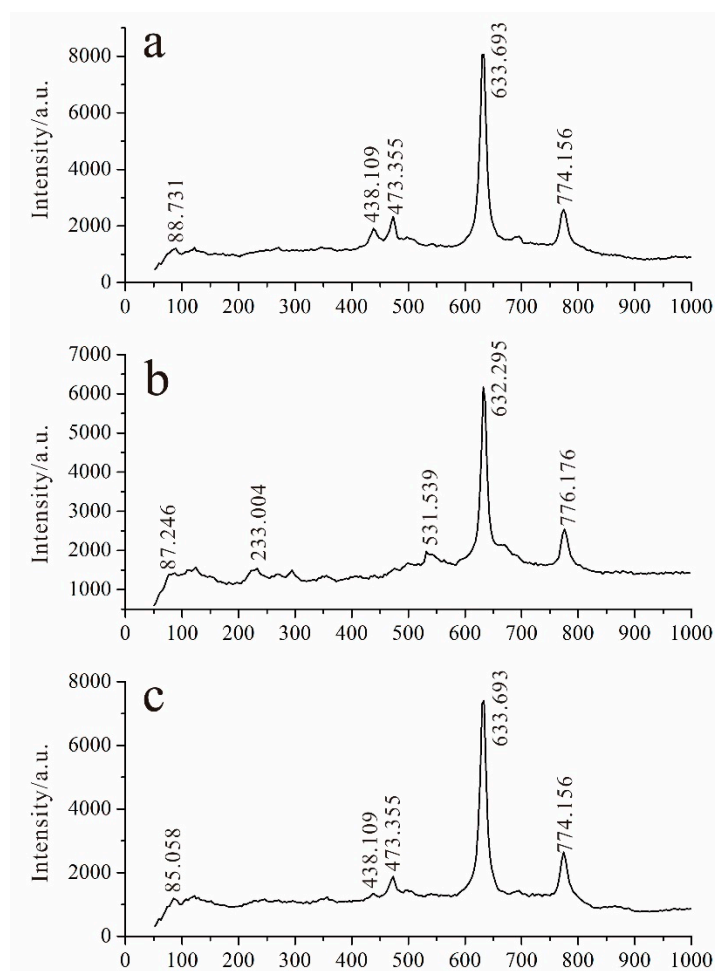


Figure 6. Measured Raman spectra of different cassiterite samples. (a) is XA-3, (b) is XA-4, (c) is XA-5.

5.3. Cassiterite Composition

Trace element contents of cassiterite are listed in Table 3. The average SnO_2 contents of XA-3, XA-4, and XA-5 in the study area were 99.170 wt % (96.631 wt % to 100.416 wt %), 99.037 wt % (96.516 wt % to 100.022 wt %), and 99.338 wt % (98.699 wt % to 99.885 wt %), respectively. The main trace elements in these different types of cassiterite comprised Fe, Nb, Ta, and Ti, and minor trace elements included W, Mn, and Si (Table 3). A summary of the EPMA data is shown in Table 4. Iron was the most abundant minor element in cassiterites (0.498 wt % to 1.181 wt %). In XA-3 and XA-4, Nb abundance was higher than Ta, while in XA-5, Ta abundance was higher. Ti was an important element in cassiterite and contents ranged from 0 to 1.448 wt %.

Table 3. Electron probe micro-analyzer (EPMA) data on cassiterites from Xi'ao Cu-Sn polymetallic deposit.

XA-3 Altered Rock-Type Ore															
	XA-3-1	XA-3-2	XA-3-4	XA-5-6	XA-3-7	XA-3-8	XA-3-9	XA-3-10	XA-3-11	XA-3-12	XA-3-13	XA-3-15	XA-3-17	XA-3-18	XA-3-20
	H	H	O	O	O	O	O	O	O	O	O	O	O	H	H
SnO ₂	100.416	98.882	99.667	99.445	99.716	98.754	99.966	99.775	96.631	98.772	98.278	98.957	99.815	100.087	98.392
WO ₃	0.000	0.667	0.047	0.487	0.387	0.017	0.161	0.080	0.082	0.031	0.030	0.029	0.000	0.000	0.037
Nb ₂ O ₅	0.000	0.058	0.192	0.000	0.024	0.038	0.010	0.039	0.558	0.019	0.005	0.063	0.039	0.029	0.592
Ta ₂ O ₅	0.000	0.014	0.255	0.000	0.000	0.277	0.000	0.213	0.000	0.000	0.000	0.047	0.000	0.000	0.110
FeO	0.625	0.782	0.626	0.744	0.678	0.501	0.498	0.530	0.712	1.168	0.952	0.721	0.876	0.653	0.621
MnO	0.023	0.032	0.015	0.024	0.000	0.016	0.000	0.006	0.002	0.005	0.000	0.000	0.000	0.002	0.000
TiO ₂	0.000	0.018	0.211	0.150	0.240	0.000	0.000	0.145	0.810	0.209	1.052	0.772	0.235	0.219	0.638
SiO ₂	0.012	0.005	0.080	0.024	0.011	0.041	0.004	0.047	0.054	0.000	0.000	0.026	0.000	0.031	0.000
Total	101.076	100.458	101.093	100.874	101.056	99.644	100.639	100.835	98.849	100.204	100.317	100.615	100.965	101.021	100.390
Cation Formula Based on Four Atoms of Oxygen															
Sn ⁴⁺	1.9795	1.9593	1.9580	1.9603	1.9615	1.9798	1.9849	1.9737	1.9327	1.9639	1.9383	1.9504	1.9700	1.9745	1.9428
W ⁶⁺	0.0000	0.0086	0.0006	0.0062	0.0049	0.0002	0.0021	0.0010	0.0011	0.0004	0.0004	0.0004	0.0000	0.0000	0.0005
Nb ⁵⁺	0.0000	0.0013	0.0043	0.0000	0.0005	0.0009	0.0002	0.0009	0.0126	0.0004	0.0001	0.0014	0.0009	0.0006	0.0133
Ta ⁵⁺	0.0000	0.0002	0.0034	0.0000	0.0000	0.0038	0.0000	0.0029	0.0000	0.0000	0.0000	0.0006	0.0000	0.0000	0.0015
Fe ²⁺	0.0388	0.0488	0.0387	0.0462	0.0420	0.0351	0.0346	0.0367	0.0498	0.0812	0.0657	0.0497	0.0605	0.0451	0.0429
Mn ²⁺	0.0010	0.0013	0.0006	0.0010	0.0000	0.0007	0.0000	0.0003	0.0001	0.0002	0.0000	0.0000	0.0000	0.0001	0.0000
Ti ⁴⁺	0.0000	0.0007	0.0078	0.0056	0.0089	0.0000	0.0000	0.0054	0.0306	0.0078	0.0391	0.0287	0.0087	0.0081	0.0238
Si ⁴⁺	0.0006	0.0003	0.0039	0.0012	0.0005	0.0020	0.0002	0.0023	0.0027	0.0000	0.0000	0.0013	0.0000	0.0015	0.0000
Total	2.0199	2.0204	2.0175	2.0205	2.0184	2.0225	2.0219	2.0232	2.0295	2.0540	2.0436	2.0324	2.0401	2.0299	2.0247
Nb + Ta	0.0000	0.0015	0.0077	0.0000	0.0005	0.0047	0.0002	0.0037	0.0126	0.0004	0.0001	0.0020	0.0009	0.0006	0.0147
Fe + Mn	0.0398	0.0501	0.0393	0.0472	0.0420	0.0358	0.0346	0.0370	0.0499	0.0814	0.0657	0.0497	0.0605	0.0452	0.0429

Table 3. Cont.

XA-4 Altered Rock-Type Ore																	
	XA-4-1	XA-4-2	XA-4-3	XA-4-4	XA-4-6	XA-4-7	XA-4-8	XA-4-9	XA-4-5	XA-4-10	XA-4-11	XA-4-12	XA-4-13	XA-4-14	XA-4-15	XA-4-16	XA-4-17
	O	O	O	H	H	H	H	H							H		
SnO ₂	98.483	99.626	99.369	99.397	99.949	99.423	98.811	99.598	96.516	98.760	99.027	98.777	99.634	99.005	98.994	98.236	100.022
WO ₃	0.062	0.065	0.000	0.052	0.011	0.000	0.037	0.000	0.087	0.143	0.000	0.000	0.042	0.000	0.000	0.547	0.012
Nb ₂ O ₅	0.029	0.000	0.039	0.000	0.106	0.067	0.000	0.082	0.513	0.250	0.005	0.000	0.000	0.086	0.000	0.077	0.038
Ta ₂ O ₅	0.047	0.077	0.000	0.000	0.000	0.019	0.000	0.049	0.339	0.184	0.000	0.025	0.000	0.000	0.118	0.093	0.000
FeO	0.614	0.680	0.965	0.597	0.521	0.800	0.795	0.553	0.959	0.588	0.587	0.751	0.656	0.606	0.802	0.606	0.590
MnO	0.028	0.000	0.028	0.000	0.007	0.000	0.000	0.000	0.000	0.019	0.011	0.000	0.015	0.000	0.014	0.000	0.000
TiO ₂	0.400	0.381	0.308	0.066	0.282	0.014	0.036	0.000	1.448	0.225	0.754	0.392	0.179	0.628	0.632	0.849	0.201
SiO ₂	0.048	0.019	0.032	0.033	0.030	0.057	0.064	0.003	0.064	0.028	0.021	0.024	0.043	0.021	0.000	0.016	0.048
Total	99.711	100.848	100.741	100.145	100.906	100.380	99.743	100.285	99.926	100.197	100.405	99.969	100.569	100.346	100.560	100.424	100.911
Cation Formula Based on Four Atoms of Oxygen																	
Sn ⁴⁺	1.9648	1.9667	1.9631	1.9810	1.9727	1.9759	1.9762	1.9838	1.8733	1.9632	1.9570	1.9662	1.9749	1.9591	1.9557	1.9394	1.9753
W ⁶⁺	0.0008	0.0008	0.0000	0.0007	0.0001	0.0000	0.0005	0.0000	0.0011	0.0018	0.0000	0.0000	0.0005	0.0000	0.0000	0.0070	0.0002
Nb ⁵⁺	0.0007	0.0000	0.0009	0.0000	0.0024	0.0015	0.0000	0.0018	0.0121	0.0056	0.0001	0.0000	0.0000	0.0019	0.0000	0.0017	0.0009
Ta ⁵⁺	0.0006	0.0010	0.0000	0.0000	0.0000	0.0003	0.0000	0.0007	0.0045	0.0025	0.0000	0.0003	0.0000	0.0000	0.0016	0.0013	0.0000
Fe ²⁺	0.0428	0.0470	0.0667	0.0416	0.0360	0.0556	0.0556	0.0386	0.0651	0.0409	0.0405	0.0523	0.0455	0.0419	0.0554	0.0418	0.0408
Mn ²⁺	0.0012	0.0000	0.0012	0.0000	0.0003	0.0000	0.0000	0.0000	0.0000	0.0008	0.0005	0.0000	0.0006	0.0000	0.0006	0.0000	0.0000
Ti ⁴⁺	0.0151	0.0142	0.0115	0.0025	0.0105	0.0005	0.0013	0.0000	0.0530	0.0084	0.0281	0.0147	0.0067	0.0234	0.0235	0.0316	0.0075
Si ⁴⁺	0.0024	0.0009	0.0016	0.0017	0.0015	0.0028	0.0032	0.0002	0.0031	0.0014	0.0010	0.0012	0.0021	0.0010	0.0000	0.0008	0.0024
Total	2.0284	2.0306	2.0448	2.0274	2.0234	2.0366	2.0368	2.0251	2.0122	2.0247	2.0272	2.0348	2.0303	2.0274	2.0368	2.0236	2.0269
Nb + Ta	0.0013	0.0010	0.0009	0.0000	0.0024	0.0018	0.0000	0.0025	0.0166	0.0081	0.0001	0.0003	0.0000	0.0019	0.0016	0.0030	0.0009
Fe + Mn	0.0440	0.0470	0.0678	0.0416	0.0362	0.0556	0.0556	0.0386	0.0651	0.0417	0.0410	0.0523	0.0461	0.0419	0.0560	0.0418	0.0408

Table 3. Cont.

XA-5 Tourmaline Vein-Type Ore																
	XA-5-6	XA-5-8	XA-5-9	XA-5-10	XA-5-11	XA-5-12	XA-5-13	XA-5-15	XA-5-16	XA-5-17	XA-5-18	XA-5-19	XA-5-20	XA-5-21	XA-5-22	XA-5-23
	O	O	O	O	H	O	O	O	O	O	O	O	O	O	O	O
SnO ₂	99.885	99.022	99.149	99.757	99.161	99.584	99.124	98.823	99.568	98.975	99.168	99.867	99.452	98.699	99.362	99.816
WO ₃	0.000	0.031	0.128	0.000	0.033	0.000	0.016	0.066	0.000	0.070	0.062	0.000	0.046	0.000	0.035	0.000
Nb ₂ O ₅	0.082	0.000	0.067	0.048	0.048	0.043	0.149	0.000	0.000	0.000	0.034	0.000	0.111	0.000	0.115	0.024
Ta ₂ O ₅	0.000	0.000	0.066	0.000	0.376	0.003	0.334	0.123	0.060	0.189	0.104	0.000	0.000	0.044	0.305	0.071
FeO	0.655	0.666	0.723	0.543	1.081	0.645	0.643	1.040	0.705	0.991	1.082	1.181	0.588	1.065	0.857	0.649
MnO	0.034	0.000	0.011	0.000	0.000	0.009	0.000	0.000	0.009	0.012	0.000	0.006	0.035	0.017	0.000	0.010
TiO ₂	0.000	0.216	0.070	0.098	0.135	0.154	0.237	0.188	0.177	0.005	0.021	0.000	0.095	0.085	0.202	0.154
SiO ₂	0.028	0.000	0.040	0.000	0.012	0.041	0.037	0.030	0.077	0.068	0.033	0.070	0.053	0.025	0.025	0.011
Total	100.684	99.935	100.254	100.446	100.846	100.479	100.540	100.270	100.596	100.310	100.504	101.124	100.380	99.935	100.901	100.735
Cation Formula Based on Four Atoms of Oxygen																
Sn ⁴⁺	1.9752	1.9704	1.9671	1.9780	1.9526	1.9707	1.9592	1.9558	1.9665	1.9608	1.9600	1.9584	1.9707	1.9612	1.9557	1.9715
W ⁶⁺	0.0000	0.0004	0.0016	0.0000	0.0004	0.0000	0.0002	0.0008	0.0000	0.0009	0.0008	0.0000	0.0006	0.0000	0.0004	0.0000
Nb ⁵⁺	0.0018	0.0000	0.0015	0.0011	0.0011	0.0010	0.0033	0.0000	0.0000	0.0000	0.0008	0.0000	0.0025	0.0000	0.0026	0.0005
Ta ⁵⁺	0.0000	0.0000	0.0009	0.0000	0.0050	0.0000	0.0045	0.0017	0.0008	0.0026	0.0014	0.0000	0.0000	0.0006	0.0041	0.0010
Fe ²⁺	0.0408	0.0417	0.0452	0.0339	0.0670	0.0402	0.0401	0.0648	0.0439	0.0618	0.0673	0.0751	0.0367	0.0666	0.0531	0.0403
Mn ²⁺	0.0014	0.0000	0.0005	0.0000	0.0000	0.0004	0.0000	0.0000	0.0004	0.0005	0.0000	0.0003	0.0015	0.0007	0.0000	0.0004
Ti ⁴⁺	0.0000	0.0081	0.0026	0.0037	0.0050	0.0057	0.0088	0.0070	0.0066	0.0002	0.0008	0.0000	0.0036	0.0032	0.0075	0.0057
Si ⁴⁺	0.0014	0.0000	0.0020	0.0000	0.0006	0.0021	0.0018	0.0015	0.0038	0.0034	0.0017	0.0037	0.0026	0.0013	0.0013	0.0006
Total	2.0207	2.0206	2.0214	2.0167	2.0318	2.0200	2.0180	2.0315	2.0219	2.0301	2.0327	2.0374	2.0182	2.0335	2.0246	2.0200
Nb + Ta	0.0018	0.0000	0.0024	0.0011	0.0061	0.0010	0.0078	0.0017	0.0008	0.0026	0.0022	0.0000	0.0025	0.0006	0.0067	0.0015
Fe + Mn	0.0422	0.0417	0.0456	0.0339	0.0670	0.0406	0.0401	0.0648	0.0442	0.0623	0.0673	0.0754	0.0382	0.0673	0.0531	0.0407

Table 4. Statistical characteristics of EPMA results.

Sample	SnO ₂	WO ₃	Nb ₂ O ₅	Ta ₂ O ₅	FeO	MnO	TiO ₂	SiO ₂
XA-3	99.170 ± 0.95 ^a	0.137 ± 0.21	0.111 ± 0.19	0.061 ± 0.1	0.713 ± 0.18	0.008 ± 0.01	0.313 ± 0.34	0.022 ± 0.02
	96.631–100.416 ^b	0–0.667	0–0.592	0–0.277	0.498–1.168	0–0.032	0–1.052	0–0.080
XA-4	99.037 ± 0.82	0.062 ± 0.13	0.076 ± 0.13	0.056 ± 0.09	0.686 ± 0.14	0.007 ± 0.01	0.400 ± 0.37	0.032 ± 0.02
	96.516–100.022	0–0.547	0–0.513	0–0.339	0.521–0.964	0–0.028	0–1.448	0–0.064
XA-5	99.338 ± 0.38	0.030 ± 0.04	0.045 ± 0.05	0.105 ± 0.13	0.820 ± 0.22	0.009 ± 0.01	0.115 ± 0.08	0.034 ± 0.02
	98.699–99.885	0–0.128	0–0.149	0–0.376	0.543–1.181	0–0.035	0–0.237	0–0.077

^a: mean ± sd, ^b: range of concentration.

5.4. Oxygen Isotopes

The results of oxygen isotope determination of the cassiterite samples are shown in Table 5. The cassiterite samples showed $\delta^{18}\text{O}$ values ranging from 3.9‰ to 4.7‰ (Table 5), exhibiting a gradual decrease from XA-3 to XA-4 to XA-5. The $\delta^{18}\text{O}$ values of XA-3, XA-4 and XA-5 were 4.7‰, 4.4‰ and 3.9‰, respectively. Calculating the precise $\delta^{18}\text{O}_{\text{H}_2\text{O}}$ values of fluids that were in equilibrium with cassiterite was difficult due to the large variation in temperatures obtained from fluid inclusions [50]. Here, we used the average homogenization temperatures of these fluid inclusions to calculate their $\delta^{18}\text{O}_{\text{H}_2\text{O}}$ values. The calculated $\delta^{18}\text{O}_{\text{H}_2\text{O}}$ values of these fluids were similar and within a limited range (7.16‰ to 8.25‰). The $\delta^{18}\text{O}_{\text{H}_2\text{O}}$ values of XA-3, XA-4, and XA-5 were 8.25‰, 7.95‰, and 7.16‰, respectively.

Table 5. The $\delta^{18}\text{O}$ values of cassiterite samples in Xi'ao Cu-Sn polymetallic deposit.

Samples	Minerals	$\delta^{18}\text{O}_{\text{V-PDB}}$ (‰)	$\delta^{18}\text{O}_{\text{V-SMOW}}$ (‰)	Temperature (°C) ^a	$\delta^{18}\text{O}_{\text{H}_2\text{O-SMOW}}$ (‰)
XA-3	Cassiterite	−25.40	4.7	374.10	8.25
XA-4		−25.70	4.4	374.10	7.95
XA-5		−26.20	3.9	353.82	7.16

^a, temperatures were taken from [50].

5.5. U-Pb Ages

The cassiterite grains used for U-Pb isotope analysis had a few cracks and fluid inclusions. Care was taken when selecting laser positions to avoid cracks and fluid inclusions to reduce the influence of common Pb in inclusions and to improve the accuracy of analyses. Both O and H zones were used for U-Pb dating. The LA-ICP-MS results are summarized in Table 6 and plotted in Figure 7. Figure 7 indicates that cassiterites from the XA-3, XA-4, and XA-5 yielded U-Pb Tera-Wasserburg concordia lower intercept ages of 83.3 ± 2.1 Ma (1σ , MSWD = 0.29) (MSWD: mean squares weighted deviates), 84.9 ± 1.7 Ma (1σ , MSWD = 0.78), and 84.0 ± 5.6 Ma (1σ , MSWD = 4.1), respectively. These data represent the metallogenic age of the Xi'ao Cu-Sn polymetallic deposit.

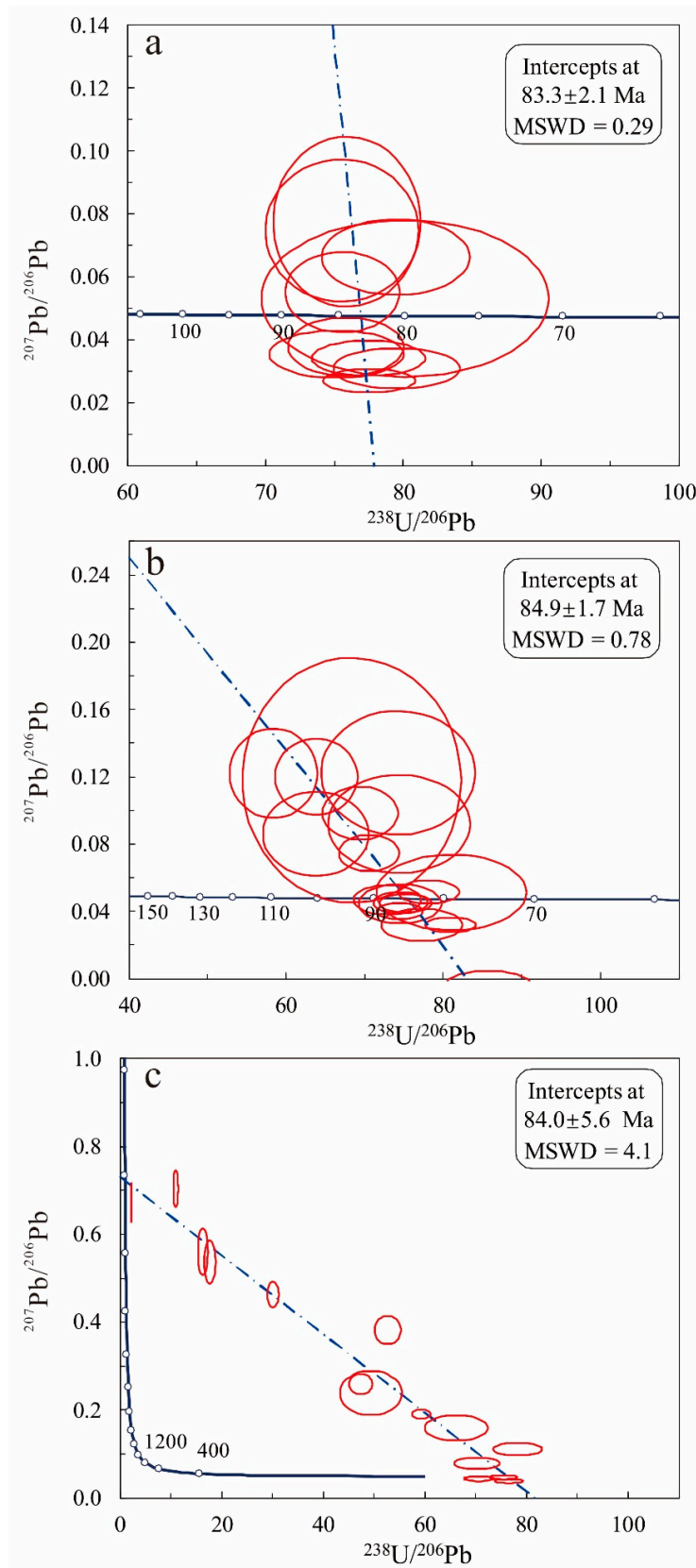


Figure 7. U-Pb Tera-Wasserburg concordia age for cassiterite samples from Xi’ao deposit. (a) is the age of XA-3, (b) is the age XA-4, (c) is the age XA-5.

Table 6. LA-ICP-MS U-Pb dating results of cassiterite from the Xi'ao Cu-Sn polymetallic deposit.

XA-3 Altered Rock-Type Ore																
Spots	Th	U	Isotopic Ratios								Age (Ma)					
			²³⁸ U/ ²⁰⁶ Pb	1σ	²⁰⁷ Pb/ ²⁰⁶ Pb	1σ	²⁰⁶ Pb/ ²³⁸ U	1σ	²⁰⁷ Pb/ ²³⁵ U	1σ	²⁰⁷ Pb/ ²⁰⁶ Pb	1σ	²⁰⁶ Pb/ ²³⁸ U	1σ	²⁰⁷ Pb/ ²³⁵ U	1σ
XA16-3-3	0	20,627	75.1314801	3.217501	0.03543	0.00497	0.01331	0.00057	0.06532	0.00877	0.1	0	85.3	3.62	64.2	8.36
XA16-3-4	8	64,216	77.5193798	2.223424	0.02693	0.00255	0.0129	0.00037	0.04806	0.00438	0.1	0	82.6	2.33	47.7	4.24
XA16-3-5	0	38,135	77.4593338	2.699977	0.03421	0.00376	0.01291	0.00045	0.06101	0.00639	0.1	0	82.7	2.86	60.1	6.11
XA16-3-6	0	32,544	79.491256	3.033053	0.031	0.00423	0.01258	0.00048	0.05385	0.00708	0.1	0	80.6	3.07	53.3	6.82
XA16-3-8	0	23,724	79.4281176	3.532942	0.06637	0.00797	0.01259	0.00056	0.11525	0.01289	818.2	232.61	80.7	3.55	110.8	11.74
XA16-3-11	0	46,501	75.8150114	2.759	0.0378	0.00616	0.01319	0.00048	0.06922	0.01094	0.1	0	84.5	3.08	68	10.39
XA16-3-12	0	51,406	80.1282051	6.869966	0.05307	0.01635	0.01248	0.00107	0.09228	0.02726	331.9	579.52	80	6.84	89.6	25.34
XA16-3-13	0	64,041	75.5857899	2.742342	0.05508	0.00849	0.01323	0.00048	0.102	0.01516	415.3	312.01	84.7	3.08	98.6	13.97
XA16-3-14	0	23,742	75.5287009	3.650934	0.07457	0.01498	0.01324	0.00064	0.13904	0.02702	1056.5	359.19	84.8	4.08	132.2	24.09
XA16-3-16	0	32,855	75.8725341	3.511551	0.07766	0.01786	0.01318	0.00061	0.14698	0.0334	1138.3	400.23	84.4	3.86	139.2	29.57
XA-4 Altered Rock-Type Ore																
Spots	Th	U	Isotopic Ratios								Ages (Ma)					
			²³⁸ U/ ²⁰⁶ Pb	1σ	²⁰⁷ Pb/ ²⁰⁶ Pb	1σ	²⁰⁶ Pb/ ²³⁸ U	1σ	²⁰⁷ Pb/ ²³⁵ U	1σ	²⁰⁷ Pb/ ²⁰⁶ Pb	1σ	²⁰⁶ Pb/ ²³⁸ U	1σ	²⁰⁷ Pb/ ²³⁵ U	1σ
XA-4-1	0	38,164	70.52186	2.5364	0.07462	0.00723	0.01418	0.00051	0.14623	0.0133	1058	183.86	90.8	3.26	138.6	11.78
XA-4-2	1	36,083	69.39625	3.178454	0.09839	0.01033	0.01441	0.00066	0.19591	0.01873	1593.9	184.1	92.2	4.18	181.7	15.9
XA-4-3	3	91,084	74.46016	1.940511	0.04016	0.00318	0.01343	0.00035	0.07453	0.00565	0.1	0	86	2.26	73	5.34
XA-4-4	0	31,407	72.83321	2.811479	0.0469	0.00583	0.01373	0.00053	0.08894	0.01058	44	273.39	87.9	3.4	86.5	9.86
XA-4-5	0	58,372	85.6898	3.597944	−0.00366	0.00568	0.01167	0.00049	−0.0059	0.00916	0.1	0	74.8	3.13	−6	9.35
XA-4-6	0	72,882	74.51565	2.276559	0.04511	0.00408	0.01342	0.00041	0.08358	0.00721	0.1	157.16	85.9	2.62	81.5	6.75
XA-4-7	0	18,842	74.46016	3.492919	0.04477	0.00769	0.01343	0.00063	0.08302	0.01377	0.1	305.34	86	3.99	81	12.91
XA-4-8	0	6665	63.77551	4.392701	0.08595	0.01659	0.01568	0.00108	0.18605	0.03366	1336.9	333.6	100.3	6.88	173.3	28.81
XA-4-9	0	11,272	63.85696	3.466055	0.12024	0.01501	0.01566	0.00085	0.25995	0.02943	1959.8	207.41	100.2	5.42	234.6	23.72
XA-4-10	0	7160	58.34306	3.676225	0.12216	0.01768	0.01714	0.00108	0.28893	0.03792	1988	237.23	109.6	6.82	257.7	29.88
XA-4-11	0	126,487	80.84074	2.156625	0.03191	0.00289	0.01237	0.00033	0.05443	0.00475	0.1	0	79.2	2.1	53.8	4.58
XA-4-12	0	5181	74.23905	6.448381	0.12237	0.02421	0.01347	0.00117	0.22732	0.04059	1991.1	315.34	86.2	7.43	208	33.58
XA-4-13	0	58,639	78.125	2.563477	0.05157	0.00471	0.0128	0.00042	0.09105	0.00785	266.4	196.22	82	2.65	88.5	7.31

Table 6. Cont.

XA-4-14	0	1704	68.3527	9.1573	0.11805	0.04805	0.01463	0.00196	0.23816	0.09165	1926.9	591.79	93.6	12.46	216.9	75.16
XA-4-15	0	9525	80.97166	6.294153	0.05115	0.01484	0.01235	0.00096	0.08714	0.02439	247.4	558.56	79.2	6.11	84.8	22.78
XA-4-16	0	6612	74.34944	5.970067	0.09207	0.01935	0.01345	0.00108	0.17076	0.03324	1468.7	354.03	86.1	6.9	160.1	28.83
XA-4-17	0	97,931	75.18797	2.20476	0.04487	0.00372	0.0133	0.00039	0.08227	0.00645	0.1	128.04	85.2	2.48	80.3	6.06
XA-4-18	0	26,046	77.27975	3.404131	0.03189	0.0063	0.01294	0.00057	0.0569	0.01097	0.1	0	82.9	3.64	56.2	10.54
XA-5 Tourmaline Vein-Type Ore																
Spots	Th	U	Isotopic Ratios								Age (Ma)					
			²³⁸ U/ ²⁰⁶ Pb	1σ	²⁰⁷ Pb/ ²⁰⁶ Pb	1σ	²⁰⁶ Pb/ ²³⁸ U	1σ	²⁰⁷ Pb/ ²³⁵ U	1σ	²⁰⁷ Pb/ ²⁰⁶ Pb	1σ	²⁰⁶ Pb/ ²³⁸ U	1σ	²⁰⁷ Pb/ ²³⁵ U	1σ
XA-5-1	57	33,209	10.9769484	0.277135	0.70382	0.02819	0.0911	0.0023	8.88783	0.30736	4738.5	56.34	562	13.59	2326.6	31.56
XA-5-2	1	20,863	70.2247191	2.958907	0.07856	0.00878	0.01424	0.0006	0.155	0.01621	1161	206.92	91.1	3.8	146.3	14.25
XA-5-4	35	30,390	30.0390508	0.776016	0.46305	0.01974	0.03329	0.00086	2.13586	0.0787	4127.7	61.84	211.1	5.33	1160.5	25.48
XA-5-5	8	25,787	49.4071146	4.027754	0.23846	0.03313	0.02024	0.00165	0.66883	0.07615	3109.7	205.5	129.2	10.44	520	46.33
XA-5-6	133	143,761	59.2417062	1.228353	0.19086	0.00774	0.01688	0.00035	0.44634	0.01674	2749.6	65.1	107.9	2.2	374.7	11.75
XA-5-7	60	27,856	17.6584849	0.763964	0.53733	0.03368	0.05663	0.00245	4.21513	0.20401	4347	88.87	355.1	14.93	1677	39.72
XA-5-8	0	125,483	75.4716981	1.822713	0.04799	0.00317	0.01325	0.00032	0.0881	0.00555	97.6	150.41	84.9	2.04	85.7	5.18
XA-5-9	23	8254	66.0938533	4.106294	0.15994	0.01956	0.01513	0.00094	0.33533	0.03576	2455.1	193.27	96.8	5.94	293.6	27.19
XA-5-10	74	112,650	78.1860829	3.239924	0.11092	0.00998	0.01279	0.00053	0.19659	0.01594	1814.6	155.02	81.9	3.38	182.2	13.52
XA-5-11	44	47,919	47.3484848	1.546897	0.25907	0.01524	0.02112	0.00069	0.75849	0.03861	3241	89.79	134.8	4.35	573.1	22.29
XA-5-12	55	32,069	52.6315789	1.717452	0.3831	0.02155	0.019	0.00062	1.00882	0.04815	3844.1	82.39	121.3	3.95	708.3	24.34
XA-5-13	40	6225	2.12417954	0.049588	0.67373	0.03003	0.47077	0.01099	43.97262	1.81795	4675.7	62.73	2486.9	48.17	3864.6	41.05
XA-5-14	31	5892	16.2839928	0.654966	0.5602	0.035	0.06141	0.00247	4.77057	0.24063	4408	88.3	384.2	15.03	1779.7	42.34
XA-5-15	0	75,871	70.5716302	1.942338	0.04468	0.00343	0.01417	0.00039	0.08782	0.00641	0.1	104.97	90.7	2.51	85.5	5.98
XA-5-16	0	151,920	76.5110941	1.873263	0.03887	0.00258	0.01307	0.00032	0.0705	0.00446	0.1	0	83.7	2.04	69.2	4.23

6. Discussion

6.1. Timing of Sn Mineralization

Cassiterite is the main ore mineral in tin polymetallic deposits; thus, directly dating cassiterite can provide precise constraints on the timing of mineralization processes. With recent improvements in analytical techniques, the LA-ICP-MS U-Pb dating of cassiterite (SnO_2) has proven to be a powerful tool for dating tin polymetallic deposits [7,12,13,15–18,72]. Li et al. [10] discussed the reliability of using LA-ICP-MS to determine the U-Pb age of cassiterite and proposed the relative merits and reliability of isochron ages, concordia ages, and Tera-Wasserburg lower intercept ages.

In this study, we applied the LA-ICP-MS technique to obtain the U-Pb chronology of cassiterites from the two types of ores (altered rock- and tourmaline vein-type ores) in the Xi'ao Cu-Sn polymetallic deposit. The $^{207}\text{Pb}/^{206}\text{Pb}$ - $^{238}\text{U}/^{206}\text{Pb}$ Tera-Wasserburg concordia lower intercept ages of 83.3 ± 2.1 Ma to 84.9 ± 1.7 Ma (Figure 7) obtained from our data agree well with those of the Kafang (one of the five deposits in Gejiu district) cassiterite (84.4 ± 2.0 Ma) obtained by Guo et al. [35], and those of the Gaosong (one of the five deposits in Gejiu district) cassiterites (83.5 ± 2.1 Ma to 85.1 ± 1.0 Ma) obtained by Guo et al. [14]. The U-Pb system in cassiterite has a high closure temperature, and cassiterite has stable chemical properties and is resistant to hydrothermal alteration. Therefore, we conclude that the timing of Sn mineralization in the Xi'ao deposit occurred at 83.3 ± 2.1 Ma to 84.9 ± 1.7 Ma.

Numerous geochronological studies have been performed on the Laoka granite. The reported U-Pb age for the Laoka equigranular biotite granite is 85.0 ± 0.85 Ma [41,43]. Furthermore, the U-Pb ages (83.3 to 84.9 Ma) of the cassiterites obtained in our study are consistent with the previously mentioned ages, which indicates that the altered rock- and tourmaline vein-type ores in the Xi'ao Cu-Sn polymetallic deposit have a close temporal relationship with the Late Cretaceous granitic magmatism.

6.2. Color, CL Images and Raman Spectrum

The color variation of cassiterite has been attributed to elemental isomorphous substitution in the mineral lattice [7,73,74], or Fe content [75,76] or $\text{Fe}^{2+}/\text{Fe}^{3+}$ ratio [77]. However, in our cassiterites collected from Xi'ao deposit, there were no obvious relationships between Fe + Nb + Ta + Ti, Fe, or W contents and the color variation (Figure 8). Moreover, previous studies also show W and U contents are the main factors controlling the color variation of Gaosong cassiterites [14,78,79]. Both of the results illustrate other mechanisms may exist, which still need further study.

Some studies show Fe, Ti, and W contents are related to the luminescence intensity [80–84]. Figure 5 shows that the O units had elevated Ti content, and the H units usually had no or little Ti. The W content had no distinct relation with luminescence intensity. Therefore, the Ti content played an important role in the luminescence intensity of CL images of the Xi'ao cassiterites. In addition, A_{1g} was one of the characteristic peaks of cassiterite, whose Raman frequency could be significantly affected by impurities [69–71,85]. In Figure 6, low-frequency drift of A_{1g} may have been caused by the substitution of Sn by Nb, Ta, Fe, and Mn [70].

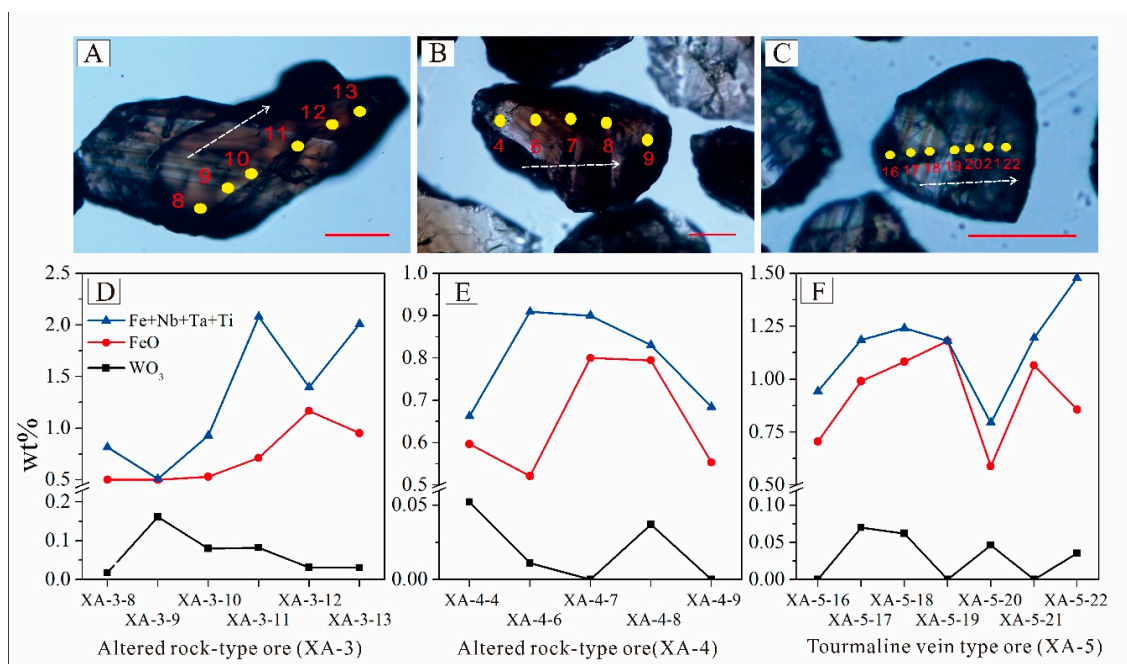


Figure 8. Relations between color and WO_3 , Fe, and Fe + Nb + Ta + Ti contents in different types of cassiterite samples. (A,D) are XA-3; (B,E) are XA-4; (C,F) are XA-5.

6.3. Metallogenic Conditions

The $\delta^{18}O$ values of cassiterite samples were indistinguishable and exhibited a narrow range from 3.9‰ to 4.7‰. The $\delta^{18}O_{H_2O}$ values were calculated using the formula based on the $\delta^{18}O$ values of cassiterite that may represent the $\delta^{18}O$ values of ore-forming fluid, which were in the range from 7.16‰ to 8.25‰. The oxygen isotope data are consistent with the values of magmatic water ($\delta^{18}O_{H_2O} = 5.5‰$ to 9.5‰) proposed by Ohmoto [86] and Sheppard [87]. Additionally, previous studies of rocks and ore minerals from the Gejiu district have reported oxygen isotopic compositions (Table 7): the whole-rock $\delta^{18}O$ of Laoka granite was 11.85‰ [88], and the calculated $\delta^{18}O_{H_2O}$ of Laoka granite was 9.3‰ [57], the $\delta^{18}O_{\text{biotite}}$ of Laoka granite was 8.58‰ [88]; the $\delta^{18}O$ values of Gejiu Formation carbonate rock limestone, marble, and dolomite were 27.31‰, 22.25‰, and 18.70‰, respectively [89]. The $\delta^{18}O_{H_2O}$ values of cassiterite samples are consistent with the calculated $\delta^{18}O_{H_2O}$ of Laoka granite rather than those of carbonate, and the H-O isotopic data of quartz in different mineralization stages indicate that ore-forming fluids were mostly derived from magma as well as the late-stage addition of meteoric water [50,88]. Therefore, we conclude that the ore-forming fluids were derived from magmatic hydrothermal system.

Table 7. The $\delta^{18}O$ of other geological samples in Xi’ao Cu-Sn polymetallic deposit.

Samples	Minerals	$\delta^{18}O_{\text{mineral}}$ (‰)	Reference
Laoka granite	Whole rock (4)	11.85	[88]
	Biotite (2)	8.58	
	Quartz	12.40	
Ore-bearing quartz vein	Quartz	12.60	[88]
Gejiu Formation limestone	Limestone	27.31	[89]
Gejiu Formation marble	Marble (2)	22.25	
Gejiu Formation dolomite	Dolomite	18.70	
Basalt amygdala	calcite	19.29	

Numerous studies have analyzed the geochemistry of cassiterites from different metallogenic environments and have observed systematic variations in their chemical compositions [3,90,91]. Cassiterites from the Xi'ao deposit had high Fe and Mn contents, which plot in the field of hydrothermal cassiterites (Figure 9). The Fe and Mn contents of cassiterites from the Xi'ao deposit were obviously higher than those of cassiterites from the Gaosong deposit. The $(\text{Ta} + \text{Nb})/(\text{Fe} + \text{Mn})$ atomic ratio of cassiterite samples varied greatly, and all data fell above the line of $(\text{Ta} + \text{Nb})/(\text{Fe} + \text{Mn}) = 1$ (Figure 9). This result could be attributed to the excess Fe present in most cassiterite samples (Table 3). The $(\text{Ta} + \text{Nb})/(\text{Fe} + \text{Mn})$ atomic ratios and their correlations demonstrate that various charge compensation mechanisms occur when Sn^{4+} is substituted [4,90]. The cations could be incorporated into the cassiterite structure according to the equation $3\text{Sn}^{4+} = (\text{Fe}, \text{Mn})^{2+} + 2(\text{Nb}, \text{Ta})^{5+}$ and $2\text{Sn}^{4+} = \text{Fe}^{3+} + (\text{Nb}, \text{Ta})^{5+}$ [74,90]. The remaining Fe would then be incorporated into the crystal by the substitutions $\text{Sn}^{4+} = \text{Fe}^{3+} + \text{H}^+$, $\text{Sn}^{4+} + \text{O}^{2-} = \text{Fe}^{3+} + \text{OH}^-$ [90], and Ti would be incorporated by the mechanism of $\text{Sn}^{4+} = \text{Ti}^{4+}$.

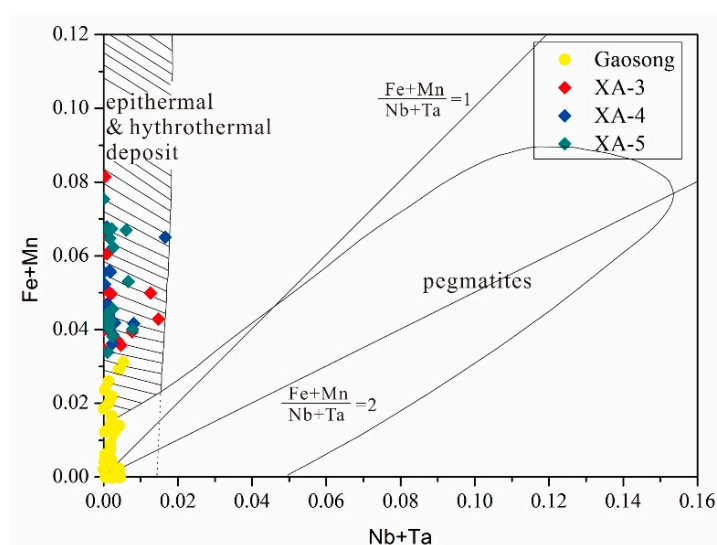


Figure 9. Covariation plot of Nb + Ta with Fe + Mn in cassiterite grains from the Xi'ao Cu-Sn deposit (EPMA data) (modified from [14]).

The trace element concentrations of cassiterites can provide information about the ore-forming fluid. For example, the high field strength elements (HFSEs, Nb, Ta, and Ti) contents of the cassiterites related to magmatic hydrothermal fluids are elevated when compared to those of cassiterites associated with sedimentary or metamorphic hydrothermal fluids [2,6,7,92,93]; for example, studies have shown that in the Furong tin deposit, HFSE concentrations of cassiterite in granite are high (Sc: 2.81~22.9 ppm; Ti: 81.1~1952 ppm; Nb: 8.94~1046 ppm; and Ta: 0.063~74.0 ppm). In contrast, cassiterite in carbonate rock, which is greatly influenced by country rock, has less Sc (0.181~1.80 ppm), Ti (3.44~75.2 ppm), Nb (0.002~0.129 ppm), and Ta (0.001~0.022 ppm) [7]. Cassiterite collected from a magmatic hydrothermal tin deposit related to granite in northern Portugal contains high contents of Nb_2O_5 (0.05 wt %~1.12 wt %), Ta_2O_5 (0.23 wt %~2.37 wt %), and TiO_2 (0.24 wt %~0.45 wt %) [6]. Cassiterite collected from the Yunlong metamorphic hydrothermal tin deposit contains low contents of HFSEs, e.g., Nb (0.17 ppm ~0.31 ppm), Ta (0.07 ppm~0.09 ppm), Sc (2.34 ppm ~2.48 ppm), and Ti (115~128 ppm) [2]. All of our studied samples contained relatively higher contents of Nb_2O_5 (0~0.592 wt %), Ta_2O_5 (0~0.376 wt %), and TiO_2 (0~1.448 wt %) (Table 3), indicating that the sources of the ore-forming fluid are enriched in HFSEs. The contents of HFSEs were high in the Laoka granite (Nb: 53.86 ppm, Ta: 19.4 ppm; Ti: 179.85 ppm [94]) but very low in the Gejiu Formation carbonate rocks, both of which are related to the Laochang tin polymetallic deposit [57,94]. Hence, the high contents of HFSEs in cassiterites may be derived from the Laoka granite, and these cassiterites likely formed in a metallogenic environment that was largely affected by granitic magma. In addition, as shown in

Table 8, the S isotopic compositions of different sulfide minerals (pyrrhotite, arsenopyrite, chalcopyrite) indicate that their $\delta^{34}\text{S}$ values (-0.2‰ ~ 2.9‰ , [38,94]) fall within the range of the $\delta^{34}\text{S}$ values for granite (-3.7‰ to 0.1‰ , [23]), which is obviously lower than that of the Gejiu Formation carbonate rock (7.14‰ to 11.1‰ , [57]), and interpreted to be of magmatic origin. All of the above data demonstrate that the Laoka granite provided the source material for tin mineralization.

Table 8. Composition of sulfur isotope in the Xi'ao Cu-Sn polymetallic deposit.

Minerals	$\delta^{34}\text{S}_{\text{V-CDT}}$ (‰)	Reference
Laoka granite	$-3.7\sim 0.1$	[23]
Carbonate	$7.4\sim 11.1$	[57]
Pyrrhotite	-0.2	[94]
Chalcopyrite	1.9	
Pyrrhotite	0.2	
Arsenopyrite	2.2	[38]
Chalcopyrite	2.9	

As important carriers of Sn, W, and other metal elements, F and Cl play a key role in the separation, migration, and enrichment of Sn, W, and HFSEs (e.g., Nb, Ta, Ti) from melt. Studies have shown that the solubilities of Nb and Ta significantly improve in fluoride solutions [95,96], as does that of Ti; these solubilities are 20–200 times higher in fluoride solutions than in pure water [97]. Within a reducing environment, the solubility of Sn in fluid can obviously increase due to the fact that Sn^{2+} and Cl^- can form more stable complexes [98,99]. The Laoka granite is peraluminous, highly evolved, and fractionated, and has a high fluorine content of 2500 ppm and a high F/Cl value (8.26) [41–43,56]. The abundance of fluorite associated with these ores also supports the interpretation that the ore-forming fluid contained a considerable amount of fluorine. Hence, fluorite mineralization is attributed to low pH and copious availability of Ca^{2+} derived from dissolution of the host limestone [100]. Under these conditions, it can be inferred that F^- beside Cl^- played possible roles as relevant complexing agents of Sn. Previous studies have shown that, during magmatic differentiation, fluorine preferentially enters the melt until it becomes saturated in a liquid phase due to its highly incompatible behavior [50,101]. Meanwhile, fluorine may also decrease the viscosity, density, and solidus temperature of magma, thus extending the length of fractional crystallization and facilitating the extraction of tin, copper, and other ore-forming elements in the residual liquid phase [101–103]. The value of D_{F} fluid/melt increases exponentially with increasing F content in the melt [104]; thus, the F content of the exsolved fluid from the F-rich melt should be high. During the late stage evolution of a F-rich magma, the ore-forming fluid formed, which was enriched in metallogenic elements (e.g., Sn, W) and HFSEs (e.g., Nb, Ta, Ti). As the ore-forming fluid migrated upward, it interacted with the Gejiu Formation carbonate rocks and was accompanied by the addition of meteoric water during the late metallogenic stage—this resulted in the formation of cassiterites with high contents of HFSEs in different regions.

6.4. Ore Genesis of the Xi'ao Deposit

At present, most large and superlarge tin deposits are of magmatic hydrothermal origin and are closely temporally and spatially associated with granites [105–107]. However, tin deposits that record other geneses, such as the Portugal Neves Corvo VMS Cu-Sn deposit [108,109] and the China Yunnan Yunlong metamorphic hydrothermal tin deposit have also been found [2]. To the best of our knowledge, deposits of types similar to the Xi'ao tin deposits described here have not been reported previously. This deposit allows us to study cassiterite mineralization more comprehensively. In this study, the colors, Raman spectra, elemental compositions, oxygen isotope results, and U-Pb geochronology indicate that the cassiterites from the Xi'ao deposit formed in the Late Cretaceous and are genetically related to Laoka biotite granite.

The ore bodies of the Xi'ao Cu-Sn polymetallic deposit are hosted within the granite, which extends to 400 m. In addition, the fluorite and the potassic alterations in the ore bodies suggest that the fluid system is rich in potassium and fluorine. The sulfur and oxygen isotopes characteristic of the sulfides and cassiterite indicate a magmatic origin [38,57,88,94]. Thus, the Xi'ao deposit may be classified as a magmatic hydrothermal deposit. Moreover, the younger U-Pb ages for the cassiterites reported here compared to the age of the Laoka granite corroborates this interpretation. The occurrence and alteration of the ore bodies provide useful information for exploring the altered rock-type Cu-Sn polymetallic deposit in Xi'ao.

7. Conclusions

The U-Pb Tera-Wasserburg concordia lower intercept ages of two samples of altered rock-type ore and one sample of tourmaline vein-type ore in the Xi'ao Cu-Sn polymetallic deposit are 83.3 ± 2.1 Ma, 84.9 ± 1.7 Ma, and 84.0 ± 5.6 Ma, respectively. These ages are highly consistent with the U-Pb age of Laoka granite, which indicates that mineralization has a close temporal relationship with the Late Cretaceous granitic magmatism. The peak values of A_{1g} were shifted to a lower frequency, possibly due to the substitution of Sn by Nb, Ta, Fe, and Mn. The $\delta^{18}O$ values of cassiterite samples and the $\delta^{18}O_{H_2O}$ values of ore-forming fluid indicate that ore-forming fluids were mostly derived from magma. The high Fe and Mn contents show that the cassiterites belong to hydrothermal cassiterites. The Nb, Ta, and Ti contents indicate that cassiterites in the Xi'ao deposit likely formed in a metallogenic environment that was largely affected by granitic magma. The later-stage hydrothermal activity dominated by Cl- and F-rich fluids was responsible for cassiterite deposition. Thus, we conclude that the Xi'ao deposit is a magmatic hydrothermal deposit.

Author Contributions: Conceptualization, Y.Z. and S.C.; Investigation, Y.Z., S.C., Y.H., J.Z., X.T. and X.C.; Data curation, Y.Z.; Formal analysis, Y.Z.; Funding acquisition, S.C.; Project administration, S.C.; Writing—original draft preparation, Y.Z.; Writing—review and editing, Y.Z. and S.C.

Funding: This work was financially supported by the National Key R&D Program of China (2016YFC0600509); a project funded by China Geological Survey (DD2016005232); and the National Natural Science Foundation of China (91755208).

Acknowledgments: We thank Shuiyuan Yang and Kuidong Zhao in Geological Processes and Mineral Resources (GPMA) for assistance with data processing and interpretation. We want to thank Huan Tian for improving the presentation of the early version of the manuscript. We are also grateful for the reviewer's constructive comments and suggestions.

Conflicts of Interest: The authors declare no conflict of interest. No potential conflict of interest was reported by the authors.

References

1. Plimer, I.R.; Lu, J.; Kleeman, J.D. Trace and rare earth elements in cassiterite-sources of components for the tin deposits of the Mole Granite, Australia. *Miner. Depos.* **1991**, *26*, 267–274. [[CrossRef](#)]
2. Jiang, S.Y.; Yu, J.M.; Lu, J.J. Trace and rare-earth element geochemistry in tourmaline and cassiterite from the Yunlong tin deposit, Yunnan, China: Implication for migmatitic-hydrothermal fluid evolution and ore genesis. *Chem. Geol.* **2004**, *209*, 193–213. [[CrossRef](#)]
3. Moore, F.; Howie, R.A. Geochemistry of some Cornubian cassiterites. *Miner. Depos.* **1979**, *14*, 103–107. [[CrossRef](#)]
4. Murciego, A.; Sanchez, A.G.; Dusauso, Y.; Pozas, J.M.M.; Ruck, R. Geochemistry and EPR of cassiterites from the Iberian Hercynian Massif. *Mineral. Mag.* **1997**, *61*, 357–365. [[CrossRef](#)]
5. Neiva, A.M.R. Geochemistry of cassiterite and its inclusions and exsolution products from tin and tungsten deposits in Portugal. *Can. Mineral.* **1996**, *34*, 745–768.
6. Neiva, A.M.R. Geochemistry of cassiterite and wolframite from tin and tungsten quartz veins in Portugal. *Ore Geol. Rev.* **2008**, *33*, 221–238. [[CrossRef](#)]

7. Wang, Z.Q.; Chen, B.; Ma, X.H. In situ LA-ICP-MS U-Pb age and geochemical data of cassiterite of the Furong tin deposit, the Nanling Range: Implications for the origin and evolution of the ore-forming fluid. *Chin. Sci. Bull.* **2014**, *59*, 2505–2519. (In Chinese) [[CrossRef](#)]
8. Zhang, D.L.; Peng, J.T.; Hu, R.Z.; Yuan, S.D.; Zheng, D.S. The Closure of U-Pb System in Cassiterite and its Reliability for Dating. *Geol. Rev.* **2011**, *57*, 549–554. (In Chinese)
9. Gulson, B.L.; Jones, M.T. Cassiterite: Potential for direct dating of mineral deposits and a precise age for the Bushveld complex granites. *Geology* **1992**, *20*, 355–358. [[CrossRef](#)]
10. Li, C.Y.; Zhang, R.Q.; Ding, X.; Ling, M.X.; Fan, W.M.; Sun, W.D. Dating cassiterite using laser ablation ICP-MS. *Ore Geol. Rev.* **2016**, *72*, 313–322. [[CrossRef](#)]
11. Liu, Y.P.; Li, Z.X.; Li, H.M.; Guo, L.G.; Xu, W.; Ye, L.; Li, C.Y.; Pi, D.H. U-Pb geochronology of cassiterite and zircon from the DuLong Sn-Zn deposit: Evidence for Cretaceous large-scale granitic magmatism and mineralization events in southeastern Yunnan province, China. *Acta Petrol. Sin.* **2007**, *23*, 967–976. (In Chinese)
12. Wang, X.J.; Liu, Y.P.; Liao, Y.L.; Bao, T.; Ye, L.; Zhang, Q. In-situ LA-MC-ICP-MS cassiterite U-Pb dating of Dulong Sn-Zn polymetallic deposit and its significance. *Acta Pet. Sin.* **2014**, *30*, 867–876. (In Chinese)
13. Yuan, S.D.; Peng, J.T.; Hu, R.Z.; Li, H.M.; Shen, N.P.; Zhang, D.L. A precise U-Pb age on cassiterite from the Xianghualing tin-polymetallic deposit (Hunan, South China). *Miner. Depos.* **2008**, *43*, 375–382. [[CrossRef](#)]
14. Guo, J.; Zhang, R.Q.; Li, C.Y.; Sun, W.D.; Hu, Y.B.; Kang, D.M.; Wu, J.D. Genesis of the Gaosong Sn-Cu deposit, Gejiu district, SW China: Constraints from in situ LA-ICP-MS cassiterite U-Pb dating and trace element fingerprinting. *Ore Geol. Rev.* **2018**, *92*, 627–642. [[CrossRef](#)]
15. Zhang, R.Q.; Lehmann, B.; Seltnann, R.; Sun, W.D.; Li, C.Y. Cassiterite U-Pb geochronology constrains magmatic-hydrothermal evolution in complex evolved granite systems: The classic Erzgebirge tin province (Saxony and Bohemia). *Geology* **2017**, *45*, 1095–1098. [[CrossRef](#)]
16. Zhang, R.Q.; Lu, J.J.; Lehmann, B.; Li, C.Y.; Li, G.L.; Zhang, L.P.; Guo, J.; Sun, W.D. Combined zircon and cassiterite U-Pb dating of the Piaotang granite-related tungsten-tin deposit, southern Jiangxi tungsten district, China. *Ore Geol. Rev.* **2017**, *82*, 268–284. [[CrossRef](#)]
17. Zhang, R.Q.; Lu, J.J.; Wang, R.C.; Yang, P.; Zhu, J.C.; Yao, Y.; Gao, J.F.; Li, C.; Lei, Z.H.; Zhang, W.L.; et al. Constraints of in situ zircon and cassiterite U-Pb, molybdenite Re-Os and muscovite ^{40}Ar - ^{39}Ar ages on multiple generations of granitic magmatism and related W-Sn mineralization in the Wangxianling area, Nanling Range, South China. *Ore Geol. Rev.* **2015**, *65*, 1021–1042. [[CrossRef](#)]
18. Yuan, S.D.; Peng, J.T.; Hao, S.; Li, H.M.; Geng, J.Z.; Zhang, D.L. In situ LA-MC-ICP-MS and ID-TIMS U-Pb geochronology of cassiterite in the giant Furong tin deposit, Hunan Province, South China: New constraints on the timing of tin-polymetallic mineralization. *Ore Geol. Rev.* **2011**, *43*, 235–242. [[CrossRef](#)]
19. Zhang, J.B.; Ding, J.H.; Nan, G.L. The characteristics and potential of tin resources in China. *Geol. Chin.* **2015**, *42*, 839–852. (In Chinese)
20. Chen, Y.X.; Li, H.; Sun, W.D.; Ireland, T.; Tian, X.F.; Hu, Y.B.; Yang, W.B.; Chen, C.; Xu, D.R. Generation of late mesozoic qianlishan A₂-type granite in Nanling Range: Implications for Shizhuyuan W-Sn mineralization and tectonic evolution. *Lithos* **2016**, *266–267*, 435–452. [[CrossRef](#)]
21. Bucci, L.A.; McNaughton, N.J.; Fletcher, I.R.; Groves, D.I.; Kositcin, N.; Stein, H.J.; Hagemann, S.G. Timing and duration of high-temperature gold mineralization and spatially associated granitoid magmatism at Chalice, Yilgarn craton, western Australia. *Econ. Geol.* **2004**, *99*, 1123–1144. [[CrossRef](#)]
22. Chen, X.C.; Hu, R.Z.; Bi, X.W.; Li, H.M.; Lan, J.B.; Zhao, C.H.; Zhu, J.J. Cassiterite LA-MC-ICP-MS U/Pb and muscovite ^{40}Ar / ^{39}Ar dating of tin deposits in the Tengchong-Lianghe tin district, NW Yunnan, China. *Miner. Depos.* **2014**, *49*, 843–860. [[CrossRef](#)]
23. Cheng, Y.B.; Mao, J.W.; Rusk, B.; Yang, Z.X. Geology and genesis of Kafang Cu-Sn deposit, Gejiu district, SW China. *Ore Geol. Rev.* **2012**, *48*, 180–196. [[CrossRef](#)]
24. Cheng, Y.B.; Mao, J.W.; Chang, Z.S.; Pirajno, F. The origin of the world class tin-polymetallic deposits in the Gejiu district, SW China: Constraints from metal zoning characteristics and ^{40}Ar - ^{39}Ar geochronology. *Ore Geol. Rev.* **2013**, *53*, 50–62. [[CrossRef](#)]
25. Qin, D.X.; Liu, Y.S.; Tan, S.C.; Chen, A.B.; Xue, C.D.; Fan, Z.G.; Dang, Y.T.; Tong, X.; Wu, J.D.; Li, Y.X.; et al. Metallogenic ages of Gejiu tin ore deposit in Yunnan Province. *Chin. J. Geol.* **2006**, *41*, 122–132. (In Chinese)

26. Yang, Z.X.; Mao, J.W.; Chen, M.H.; Tong, X.; Wu, J.D.; Cheng, Y.B.; Zhao, H.J. Re-Os dating of molybdenite from the Kafang skarn copper (tin) deposit in the Gejiu tin polymetallic ore district and its geological significance. *Acta Pet. Sin.* **2008**, *24*, 1937–1944. (In Chinese)
27. Qin, D.X.; Li, Y.S.; Fan, Z.G.; Chen, A.B.; Tan, S.C.; Hong, T.; Li, L.J.; Lin, X.P. The geochemistry and mineralization evolution of Gejiu tin ore deposits. *Eng. Sci.* **2006**, *8*, 30–39. (In Chinese)
28. Li, B.L.; Zhu, D.Q.; Xing, X.F.; Zhao, L.; Jia, L.H.; Liu, Y.H. $^{40}\text{Ar}/^{39}\text{Ar}$ geochronologic study of mica in the Gejiu tin-copper polymetallic ore district, Yunnan province, and its geological significance. *Geol. Bull. China* **2015**, *34*, 2315–2324. (In Chinese)
29. Chen, S.Y.; Zhao, P.D.; Tong, X.; Wu, J.D.; Mo, G.P.; Chen, X.S. Metallogenic characteristics of western low altered tin-copper polymetallic deposit and its prospecting significance in east part of Gejiu, Yunnan. *Earth Sci. J. China Univ. Geosci.* **2011**, *36*, 277–281. (In Chinese)
30. Chen, S.Y.; Zhao, P.D.; Tong, X.; Wu, J.D.; Mo, G.P. Mineralizing multiformity and deep prospecting of Gejiu Super Sn-Cu multi-metal deposit, Yunnan, China. *Earth Sci. J. China Univ. Geosci.* **2009**, *34*, 319–324. (In Chinese)
31. Lü, M.; Tan, S.C.; Hao, S.; Li, H.M.; Zhang, Y.H.; Chen, K.Z.; Guo, X.Y. Mineralogical study of cassiterite grains from the Gejiu tin deposit. *Northwest. Geol.* **2016**, *49*, 101–108. (In Chinese)
32. Shi, T.Z. Typomorphic features of cassiterite crystals in Gejiu Laochang deposit and its significance for determining the genetic type of deposit and finding ore shoot in Laochang deposit. *Yunnan Metall.* **1980**, *45–48*, 64. (In Chinese)
33. Shi, T.Z. Typomorphic features of cassiterite crystals in Lao-chang mining area and their geological significance. *Geochimica* **1980**, *2*, 200–205. (In Chinese)
34. Yin, C.Y. The typomorphic characteristic of cassiterites and its application in the study of the source of placer tin deposit. *Geol. Prosp.* **1981**, *11*, 24–27. (In Chinese)
35. Guo, J.; Zhang, R.Q.; Sun, W.D.; Li, C.Y. LA-ICP-MS U-Pb geochronology of cassiterite in the Gejiu tin-polymetallic deposit, Yunnan province. *Acta Mineral. Sin.* **2015**, *s1*, 698. (In Chinese)
36. Cheng, Y.B.; Spandler, C.; Kemp, A.; Mao, J.W.; Rusk, B.; Hu, Y.; Blake, K. Controls on cassiterite (SnO_2) crystallization: Evidence from cathodoluminescence, trace-element chemistry, and geochronology at the Gejiu Tin District. *Am. Mineral.* **2019**, *104*, 118–129. [[CrossRef](#)]
37. Southwest Metallurgical Geological Prospecting Company, Ministry of Metallurgical Industry. *Geology of Tin Deposits in the Gejiu Area*, 1st ed.; Metallurgical Industry Publishing House: Beijing, China, 1984; pp. 1–100. (In Chinese)
38. Zhuang, Y.Q.; Wang, R.Z.; Yang, S.P.; Yin, J.M. *Gejiu Tin (Cu) Polymetallic Ore Deposit in Yunnan*; Seismological Press House: Beijing, China, 1996; pp. 1–184. (In Chinese)
39. Wang, Q.; Li, J.W.; Jian, P.; Zhao, Z.H.; Xiong, X.L.; Bao, Z.W.; Xu, J.F.; Li, C.F.; Ma, J.L. Alkaline syenites in eastern Cathaysia (South China): Link to Permian–Triassic transtension. *Earth Planet. Sci. Lett.* **2005**, *230*, 339–354. [[CrossRef](#)]
40. Mao, J.W.; Cheng, Y.B.; Guo, C.L.; Yang, Z.X.; Feng, J.R. Gejiu tin polymetallic ore-field: Deposit model and discussion for several points concerned. *Acta Geol. Sin.* **2008**, *82*, 1455–1467. (In Chinese)
41. Cheng, Y.B.; Mao, J.W.; Xie, G.Q.; Chen, M.H.; Zhao, C.S.; Yang, Z.X.; Zhao, H.J.; Li, X.Q. Petrogenesis of the Laochang-Kafang granite in the Gejiu Area, Yunnan Province: Constraints from geochemistry and zircon U-Pb dating. *Acta Geol. Sin.* **2008**, *82*, 1478–1493. (In Chinese)
42. Cheng, Y.B.; Mao, J.W.; Xie, G.Q.; Chen, M.H.; Yang, Z.X. Zircon U-Pb dating of granites in Gejiu superlarge tin polymetallic orefield and its significance. *Miner. Depos.* **2009**, *3*, 297–312. (In Chinese)
43. Cheng, Y.B.; Mao, J.W. Age and geochemistry of granites in Gejiu area, Yunnan province, SW China: Constraints on their petrogenesis and tectonic setting. *Lithos* **2010**, 258–276. [[CrossRef](#)]
44. Li, X.L.; Mao, J.W.; Cheng, Y.B.; Zhang, J. Petrogenesis of the Gaofengshan granite in Gejiu area, Yunnan Province: Zircon U-Pb dating and geochemical constraints. *Acta Petrol. Sin.* **2012**, 183–198. (In Chinese)
45. Zhang, J.W.; Dai, C.G.; Huang, Z.L.; Luo, T.Y.; Qian, Z.K.; Zhang, Y. Age and petrogenesis of Anisian magnesian alkali basalts and their genetic association with the Kafang stratiform Cu deposit in the Gejiu supergiant tin-polymetallic district, SW China. *Ore Geol. Rev.* **2015**, *69*, 403–416. [[CrossRef](#)]
46. Chen, Y.C.; Zhu, Y.S. *Mineral Deposits of China*; Geological Publishing House: Beijing, China, 1993; pp. 209–211. (In Chinese)

47. Suo, S.T.; Bi, X.H.; Zhou, H.W. *Very Low Grade Metamorphism*; Geological Publishing House: Beijing, China, 1999; pp. 1–68. (In Chinese)
48. Yan, D.P.; Zhou, M.F.; Wang, Y.; Wang, C.L.; Zhao, T.P. Structural styles and chronological evidences from Dulong–Song Chay tectonic dome: Earlier spreading of south China sea basin due to late mesozoic to early cenozoic extension of south China block. *Earth Sci. J. China Univ. Geosci.* **2005**, *30*, 402–412. (In Chinese)
49. Liu, S.; Su, W.C.; Hu, R.Z.; Feng, C.X.; Gao, S.; Coulson, I.M.; Wang, T.; Feng, G.Y.; Tao, Y.; Xia, Y. Geochronological and geochemical constraints on the petrogenesis of alkaline ultramafic dykes from southwest Guizhou Province, SW China. *Lithos* **2010**, *114*, 253–264. [[CrossRef](#)]
50. Liao, S.L.; Chen, S.Y.; Deng, X.H.; Li, P.; Zhao, J.N.; Liao, R.Y.Z. Fluid inclusion characteristics and geological significance of the Xi’ao copper-tin polymetallic deposit in Gejiu, Yunnan Province. *J. Asian Earth Sci.* **2014**, *79*, 455–467. [[CrossRef](#)]
51. Wu, Q.S.; Liu, Q.L. Genetic evolution and mineralization of Gejiu tin-bearing granite. *Miner. Resour. Geol.* **1985**, *4*, 22–31. (In Chinese)
52. Wu, Q.S.; Liu, Q.L. Genesis, evolution and mineralization of a complex formed from Sn-bearing granite magma in Gejiu, Yunnan. *J. Guilin Coll. Geol.* **1986**, *6*, 229–238. (In Chinese)
53. Cheng, Y.B.; Mao, J.W.; Chen, M.H.; Yang, Z.X.; Feng, J.R.; Zhao, H.J. LA-ICP-MS zircon dating of alkaline rocks and lamprophyres in Gejiu area and its implications. *Geol. Chin.* **2008**, *35*, 1138–1149. (In Chinese)
54. Zhang, Y.; Huang, Z.L.; Luo, T.Y.; Qian, Z.K.; Zhang, J.W.; Sun, J.B. The geochemistry and geochronology of the Jiasha intrusion. *Geochimica* **2013**, *42*, 523–543. (In Chinese)
55. Lü, B.S. A new round of mineral prospecting and prospecting targets in Gejiu, Yunnan province. *Geol. Rev.* **2005**, *51*, 640–648. (In Chinese)
56. Li, J.H. Study of origin and characteristics of the granite in Gejiu Sn deposits. *Yunnan Geol.* **1985**, *4*, 327–352. (In Chinese)
57. Qin, D.X.; Li, Y.S. *Studies on the Geology of the Gejiu Sn-Cu Polymetallic Deposit*; Science Press: Beijing, China, 2008; pp. 1–180. (In Chinese)
58. Liao, S.L.; Chen, S.Y.; Deng, X.H.; Li, P. REE characteristics and significance of granite alteration zone of Xi’ao copper-tin polymetallic deposit in Gejiu area. *J. Cent. South Univ.* **2014**, *45*, 1555–1565. (In Chinese)
59. Liao, S.L.; Chen, S.Y.; Yao, T.; Zhao, J.N.; Deng, X.H.; Li, P. Geochemical characteristics and Geological significance of the Xi’ao Cu-Sn polymetallic deposit in the Gejiu area. *Geotecton. Metall.* **2014**, *38*, 635–646. (In Chinese)
60. Zhang, R.X.; Yang, S.Y. A mathematical model for determining carbon coating thickness and its application in electron probe microanalysis. *Microsc. Microanal.* **2016**, *22*, 1374–1380. [[CrossRef](#)]
61. Clayton, R.N.; O’Neil, J.R.; Mayeda, T.K. Oxygen isotope exchange between quartz and water. *J. Geophys. Res.* **1972**, *77*, 3057–3067. [[CrossRef](#)]
62. Zhang, L.G.; Liu, J.X.; Chen, Z.S.; Zhou, H.B. Experimental investigations of oxygen isotope fractionation in cassiterite and wolframite. *Econ. Geol.* **1994**, *89*, 150–157. [[CrossRef](#)]
63. Li, C.Y.; Wang, F.Y.; Hao, X.L.; Ding, X.; Zhang, H.; Ling, M.X.; Zhou, J.B.; Li, Y.L.; Fan, W.M.; Sun, W.D. The formation of the Dabaoshan porphyry molybdenum deposit induced by slab rollback. *Lithos* **2012**, *150*, 101–110. [[CrossRef](#)]
64. Tu, X.L.; Zhang, H.; Deng, W.F.; Ling, M.X.; Liang, H.Y.; Liu, Y.; Sun, W.D. Application of RESOLUTION in-situ laser ablation ICP-MS in trace element analyses. *Geochimica* **2011**, *40*, 83–98. [[CrossRef](#)]
65. Lin, J.; Liu, Y.S.; Yang, Y.H.; Hu, Z.C. Calibration and correction of LA-ICP-MS and LA-MC-ICP-MS analyses for element contents and isotopic ratios. *Solid Earth Sci.* **2016**, *1*, 5–27. [[CrossRef](#)]
66. Liu, Y.S.; Gao, S.; Hu, Z.C.; Gao, C.G.; Zong, K.Q.; Wang, D.B. Continental and oceanic crust recycling-induced melt–peridotite interactions in the Trans-North China Orogen: U–Pb dating, Hf isotopes and trace elements in zircons from mantle xenoliths. *J. Pet.* **2010**, *51*, 537–571. [[CrossRef](#)]
67. Ludwig, K.R. *User’s manual for Isoplot/Ex*, 3rd ed.; A Geochronology Toolkit for Microsoft Excel, No. 4. Berkeley Geochronological Center, Special Publication; Berkeley Geochronological Center: Berkeley, CA, USA, 2003.
68. Huang, P.Y.; Wang, X.; Chen, J.; Ren, M.H.; Lai, G.B. Morphological and geochemical studies of the cassiterite in Taoxikeng deposit, southern Jiangxi, China. *Geol. Rev.* **2012**, *58*, 987–1000. (In Chinese)
69. Kaur, J.; Shah, J.; Kotnala, R.K.; Verma, K.C. Raman spectra, photoluminescence and ferromagnetism of pure, Co and Fe doped SnO₂ nanoparticles. *Ceram. Int.* **2012**, *38*, 5563–5570. [[CrossRef](#)]

70. Wang, R.C.; Wu, J.W. Raman Spectroscopy of Nb, Ta-rich Cassiterite in Beauvoir and Montebras Granites, France. *Chin. J. Geochem.* **1993**, *12*, 353–359. [[CrossRef](#)]
71. Katiyar, R.S.; Dawson, P.; Hargreave, M.M.; Wilkinson, G.R. Dynamics of the rutile structure. III. Lattice dynamics, infrared and Raman spectra of SnO₂. *J. Phys. C Solid State Phys.* **1971**, *4*, 2421–2431. [[CrossRef](#)]
72. Deng, X.H.; Chen, Y.J.; Bagas, L.; Zhou, H.Y.; Zheng, Z.; Yue, S.W.; Chen, H.J.; Li, H.M.; Tu, J.R.; Cui, Y.R. Cassiterite U-Pb geochronology of the Kekekaerde W-Sn deposit in the Baiganhu ore field, East Kunlun Orogen, NW China: Timing and tectonic setting of mineralization. *Ore Geol. Rev.* **2017**, *100*, 534–544. [[CrossRef](#)]
73. Goncharov, G.N.; Filatov, S.K. Typical structural features of cassiterite from Sherlovaya Gora. *Geochem. Int.* **1971**, *8*, 268–275.
74. Izoret, L.; Marnier, G.; Dusausoy, Y. Crystallochemical characterization of cassiterite from tin and tungsten deposits in Galicia, Spain. *Can. Mineral.* **1985**, *23*, 221–231. (In French)
75. Greaves, G.; Stevenson, B.G.; Taylor, R.G. Magnetic cassiterites from Herberton, North Queensland, Australia. *Econ. Geol.* **1971**, *66*, 480–487. [[CrossRef](#)]
76. Hosking, K.F.G.; Cai, H.L. The characteristics and significance of pleochromatism for cassiterites in the Southeast Asian tin belt. *Geol. Explor.* **1984**, *20*, 25–28. (In Chinese)
77. Grubb, P.L.C.; Hannaford, P. Ferromagnetism and colour zoning in some Malayan cassiterite. *Nature* **1966**, *209*, 677–678. [[CrossRef](#)]
78. Swart, P.K.; Moore, F. The occurrence of uranium in association with cassiterite, wolframite, and sulphide mineralization in South-West England. *Mineral. Mag.* **1982**, *46*, 211–215. [[CrossRef](#)]
79. Zagruzina, I.A.; Pinskii, E.M.; Savinova, I.B. Uranium in cassiterite of tin deposits. *Int. Geol. Rev.* **1987**, *29*, 94–109. [[CrossRef](#)]
80. Marshall, D.J. *Cathodoluminescence of Geological Materials*; Unwin Hyman: Boston, MA, USA, 1988; pp. 1–146.
81. Götze, J. Potential of cathodoluminescence (CL) microscopy and spectroscopy for the analysis of minerals and materials. *Anal. Bioanal. Chem.* **2002**, *374*, 703–708. [[CrossRef](#)]
82. Xu, H.F.; Cui, J.G.; Qiu, X.P. *Application of Cathodoluminescence in Petrology and Mineral Deposit Geology*; Geology Publishing House: Beijing, China, 2006; pp. 1–78. (In Chinese)
83. Hall, M.R.; Ribbe, P.H. An electron microprobe study of luminescence centers in cassiterite. *Am. Miner.* **1971**, *56*, 31–45.
84. Farmer, C.B.; Searl, A.; Halls, C. Cathodoluminescence and growth of cassiterite in the composite lodes at South Crofty Mine, Cornwall, England. *Mineral. Mag.* **1991**, *55*, 447–458. [[CrossRef](#)]
85. Ferrari, S.; Pampillo, L.G.; Saccone, F.D. Magnetic properties and environment sites in Fe doped SnO₂ nanoparticles. *Mater. Chem. Phys.* **2016**, *177*, 206–212. [[CrossRef](#)]
86. Ohmoto, H. Stable isotope geochemistry of ore deposits. *Rev. Min.* **1986**, *16*, 491–559.
87. Sheppard, S.M.F. Characterization and isotopic variations in natural waters. *Rev. Min.* **1986**, *16*, 165–183. [[CrossRef](#)]
88. Huang, F.S.; Mu, Z.G.; Chen, C.Y.; Wang, Z.F. The study of isotopic composition of oxygen, Hydrogen and carbon in granite of tin deposits, Gejiu. *Acta Petrol. Sin.* **1983**, *2*, 241–247. (In Chinese)
89. Liu, M. Research on the Metallogenia of the Granite Contact-Depression Zones in Gejiu Tin-Copper Polymetallic Deposit. Ph.D. Thesis, Central South University, Hunan, China, 2007.
90. Möller, P.; Dulski, P.; Szacki, W.; Malow, G.; Riedel, E. Substitution of tin in cassiterite by tantalum, niobium, tungsten, iron and manganese. *Geochim. Cosmochim. Acta* **1988**, *52*, 1497–1503. [[CrossRef](#)]
91. Schneider, H.J.; Dulski, P.; Luck, J.; Möller, P.; Villalpando, A. Correlation of trace element distribution in cassiterites and geotectonic position of their deposits in Bolivia. *Miner. Depos.* **1978**, *13*, 119–122. [[CrossRef](#)]
92. Tindle, A.G.; Breaks, F.W. Oxide minerals of the separation rapids rare-element granitic pegmatite group, northwestern Ontario. *Can. Mineral.* **1998**, *36*, 609–635.
93. Yu, J.M.; Jiang, S.Y. Trace element geochemistry of cassiterites from the Neves Corvo massive sulfide deposit, Portugal. *Geochimica* **2001**, *30*, 140–146. (In Chinese)
94. Cheng, Y.B. Spatial-Temporal Evolution of the Magmatism and Mineralization in the Gejiu Supergiant Sn Polymetallic District and Insights into Several Key Problems. Ph.D. Thesis, China University of Geosciences, Beijing, China, 2012.
95. Zarausky, G.P.; Korzhinskaya, V.; Kotova, N. Experimental studies of Ta₂O₅ and columbite–tantallite solubility in fluoride solutions from 300 to 550 °C and 50 to 100 MPa. *Miner. Petrol.* **2010**, *99*, 287–300. [[CrossRef](#)]

96. Wang, Y.; Li, J.; Lu, J.; Fan, W. Geochemical mechanism of Nb-, Ta-mineralization during the late stage of granite crystallization. *Geochemistry* **1982**, *1*, 175–185. [[CrossRef](#)]
97. Rapp, J.F.; Klemme, S.; Butler, I.B.; Harley, S.L. Extremely high solubility of rutile in chloride and fluoride-bearing metamorphic fluids: An experimental investigation. *Geology* **2010**, *38*, 323–326. [[CrossRef](#)]
98. Jackson, J.K.; Helgeson, H.C. Chemical and thermodynamic constraints on the hydrothermal transport and deposition of tin: I. Calculation of the solubility of cassiterite at high pressures and temperatures. *Geochim. Cosmochim. Acta* **1985**, *49*, 1–22. [[CrossRef](#)]
99. Chen, J. Experiment on solubility of cassiterite in the presence of charcoal. *Geol. Rev.* **1986**, *32*, 287–294. (In Chinese)
100. Naitza, S.; Conte, A.M.; Cuccuru, S.; Oggiano, G.; Secchi, F.; Tecce, F. A Late Variscan tin province associated to the ilmenite-series granites of the Sardinian Batholith (Italy): The Sn and Mo mineralisation around the Monte Linas ferroan granite. *Ore Geol. Rev.* **2017**, *80*, 1259–1278. [[CrossRef](#)]
101. Villemant, B.; Boudon, G. H₂O and halogen (F, Cl, Br) behaviour during shallow magma degassing processes. *Earth Planet. Sci. Lett.* **1999**, *168*, 271–286. [[CrossRef](#)]
102. Audétat, A.; Güther, D.; Heinrich, C.A. Magmatic-hydrothermal evolution in a fractionating granite: A microchemical study of the Sn-W-F-mineralized Mole Granite (Australia). *Geochim. Cosmochim. Acta* **2000**, *64*, 3373–3393. [[CrossRef](#)]
103. Hu, X.Y.; Shang, L.B.; Bi, X.W.; Hu, R.Z.; Fan, W.L.; Chen, Y.W. Experimental study on the tin partition between granitic silicate melt and coexisting aqueous fluid. *Bull. Min. Pet. Geochem.* **2007**, *26*, 359–365. (In Chinese) [[CrossRef](#)]
104. Webster, J.D.; Holloway, J.R. Partitioning of F and Cl between magmatic hydrothermal fluids and highly evolved granitic magmas. *Geol. Soc. Am. Spec. Pap.* **1990**, *246*, 21–34.
105. Heinrich, C.A. Thermodynamic predictions of hydrothermal chemistry of arsenic and their significance for the paragenetic sequence of some cassiterite-arsenopyrite-base metal sulfide deposits. *Econ. Geol.* **1986**, *81*, 511–529. [[CrossRef](#)]
106. Robb, L. *Introduction to Ore-Forming Processes*; Blackwell Publishing: Oxford, UK, 2005; pp. 1–374.
107. Taylor, R.G. *Geology of Tin Deposits*; Elsevier: Amsterdam, The Netherland, 1979; pp. 1–543.
108. Oliveira, J.T.; Pacheco, N.; Carvalho, P.; Ferreira, A. The Neves Corvo mine and the Paleozoic geology of southwest Portugal. Geology and VMS Deposits of the Iberian Pyrite belt. In *SEG Neves Corvo Field Conference, Abstracts and Program*; University of Lisbon: Lisbon, Portugal, 1997; pp. 21–71.
109. Relvas, J.M.; Tassinari, C.C.; Munhá, J.; Barriga, F.J. Multiple sources for ore-forming fluids in the Neves Corvo VHMS Deposit of the Iberian Pyrite Belt (Portugal): Strontium, neodymium and lead isotope evidence. *Miner. Depos.* **2001**, *36*, 416–427. [[CrossRef](#)]

